minerals

MDPI

Article

Effect of Karst Geomorphology on the Sedimentary Mineralization and Geochemical Distribution of Bauxite: An Example from the Xiaoyuan Area in Qingzhen, Guizhou Province

Hongcheng Mo [1,2], Ruidong Yang [1,2,*], Chaokun Luo [1,2], Xinzheng Li [1,2], Yanbing Ji [1,2,3], Guiyuan Yang [1,2], Xumei Zhou [1,2], Chuanqian Gao [1,2], Xu Hu [4] and Zhimeng Zeng [4]

1 College of Resources and Environmental Engineering, Guizhou University, Guiyang 550025, China; mo181123123@126.com (H.M.); kcluo2018@163.com (C.L.); xinzhengli@cumt.edu.cn (X.L.); vivian_ji.gy@foxmail.com (Y.J.); yangguiyuan_08@163.com (G.Y.); zhouxumei2020@126.com (X.Z.); 13035578080@163.com (C.G.)

2 Key Laboratory of Karst Georesources and Environment, Ministry of Education, Guizhou University, Guiyang 550025, China

3 State Key Laboratory of Ore Deposit Geochemistry, Institute of Geochemistry, Chinese Academy of Sciences, Guiyang 550002, China

4 115 Geological Party, Guizhou Bureau of Geology & Mineral Exploration, Qingzhen 551400, China; 18386306176@163.com (X.H.)

* Correspondence: rdyang@gzu.edu.cn

Abstract: Bauxite, in central Guizhou, is predominantly karst bauxite, but there is insufficient research on the effect of karst paleogeomorphology on bauxite development. Xiaoyuan bauxite is also a karst bauxite, and high- and low-iron bauxite deposits exist in the study area. This study conducts geological modeling of karst bauxite using controlled-source audio-frequency magnetotelluric (CSAMT) data and drill core data. The effects of karst paleogeomorphology on bauxite deposition and mineralization are evaluated by assessing karst paleogeomorphology, conducting a mineralogical analysis of drill cores at different locations, and determining the geochemical distribution characteristics of the elements in the horizontal and vertical directions. Combined with previous research results, we propose two metallogenic processes of high-iron and low-iron bauxite. The findings are significant for understanding the mechanism of bauxite formation.

Keywords: karst bauxite; terrain modeling; paleogeomorphology; mineral genesis; elemental behavior; ore-forming

check for updates

Citation: Mo, H.; Yang, R.; Luo, C.; Li, X.; Ji, Y.; Yang, G.; Zhou, X.; Gao, C.; Hu, X.; Zeng, Z. Effect of Karst Geomorphology on the Sedimentary Mineralization and Geochemical Distribution of Bauxite: An Example from the Xiaoyuan Area in Qingzhen, Guizhou Province. *Minerals* **2023**, *13*, 1013. https://doi.org/10.3390/min13081013

Academic Editors: Ali Abedini, Maryam Khosravi and Maria Boni

Received: 24 May 2023
Revised: 17 July 2023
Accepted: 27 July 2023
Published: 29 July 2023

1. Introduction

The bauxite deposits in the central Guizhou region were largely formed during the warm and humid Viséan stage of the Carboniferous [1–5]. Most are karst bauxite deposits based on bedrock lithology [6]. The tectonics, topography, climate, hydrology, rock type, and vegetation affect the formation of bauxite deposits [7–9]. However, our understanding of the effects of tectonic and geomorphic factors on bauxite formation remains limited. Observations challenge the applicability of existing stratigraphic theories based on sequential sedimentation and ore deposit science based on in-situ weathering processes [10]. This discrepancy is partly due to the constantly changing topography, which cannot be used to understand the effect of paleogeomorphology on the formation of bauxite. It is difficult to obtain topographic and geomorphological data for entire mining districts [7,9].

Previous studies used the modern surface bauxite mineralization thickness and terrain depth and concluded that high-altitude areas experienced strong weathering. These areas became the source of erosion materials, whereas negative terrain in low-altitude or high-altitude areas provided a sedimentary space for the accumulation of erosion materials [11–14]. Moreover, a modeling study of a karst basement based on large-scale drill core data showed that high-grade clastic bauxite occurs predominantly in negative terrain, and low-grade compact bauxite occurs in the center of the negative terrain [9]. However, few studies have focused on the effect of karst geomorphology on the distribution of ore deposits. Geological models based only on drill core data are imprecise, and the distribution characteristics of high-iron bauxite are not well understood. Large amounts of bauxite deposits exist underground in the Qingzhen-Xiuwen area of central Guizhou. Thus, it is critical to develop an efficient exploration method. Geophysical methods provide more accurate data and more refined geological models for discovering and exploiting bauxite deposits [10].

This study reconstructs the karst geomorphology of the Qingxudong formation of the Cambrian using the carboniferous bauxite deposit in the Xiaoyuan area of Qingzhen Town, central Guizhou Province, as an example. An analysis of geochemical data and mineral facies is conducted to determine the effect of paleokarst geomorphology on the deposition and mineralization of bauxite. The bauxite types in this area include high-iron, low-grade bauxite and low-iron, high-grade bauxite. The former occurs in high-altitude areas and is continental sedimentary bauxite. The latter occurs in low-altitude areas due to sedimentation of lagoon facies. Previous research on the mineralogy and geochronology of bauxite deposits in central Guizhou has shown that aluminum originated from the carbonate and clastic rocks of the underlying Cambrian strata [3,15,16]. Bauxite minerals in the Jiujialu Formation are primarily composed of aluminum hydroxide minerals (mainly diaspore), iron-bearing minerals (hematite, siderite), and clay minerals (kaolinite, illite, montmorillonite, and chlorite), as well as goethite, pyrite, anatase, and zircon [2]. This study used data from twenty-three drill cores and two magnetotelluric sounding and apparent resistivity profiles of the Xiaoyuan area were used to identify the fine-scale geomorphic features in the mining area. The mineral transitions and element transport during bauxite formation were identified by combining geomorphic reconstruction with mineralogical and geochemical characteristics.

2. Geological Setting

2.1. Regional Geology

The central Guizhou region was a stable, passive, and continental-margin carbonate platform sedimentary system during the late Sinian to Cambrian (Figure 1a) [17,18]. From the late Cambrian to the early Ordovician, the central Guizhou area experienced the Yunan Movement, creating an underwater uplift. At the end of the Ordovician, the Duyun Movement caused an uplift of the central Guizhou region from underwater to land, forming the Central Guizhou Uplift [17,19]. In the middle stage of the early Devonian, the seawater transgression from south to north created a sea basin in the southern Guizhou area, although the area from Hezhang County to Anshun City, Kaili City, and Sandu County remained a terrestrial environment [4]. The sea level dropped in the middle and late Devonian, but the sea water did not completely withdraw from the southern Guizhou area. Until the early Carboniferous, an ocean existed in the south, and a terrestrial environment occurred in the north of Guizhou Province [17]. After nearly 100 million years of large-scale weathering and erosion, the central Guizhou area became a karstic plain at the end of the Devonian. As seawater entered the region from south to north, aluminous rocks of the Jiujialu Formation were deposited under warm and humid climate conditions until the Mississippian Viséan [1–3]. During the early stage of the Mississippian Serpukhovian, the entire southern Guizhou region was invaded by seawater, and the Baizuo Formation was deposited on the Jiujialu Formation [20].

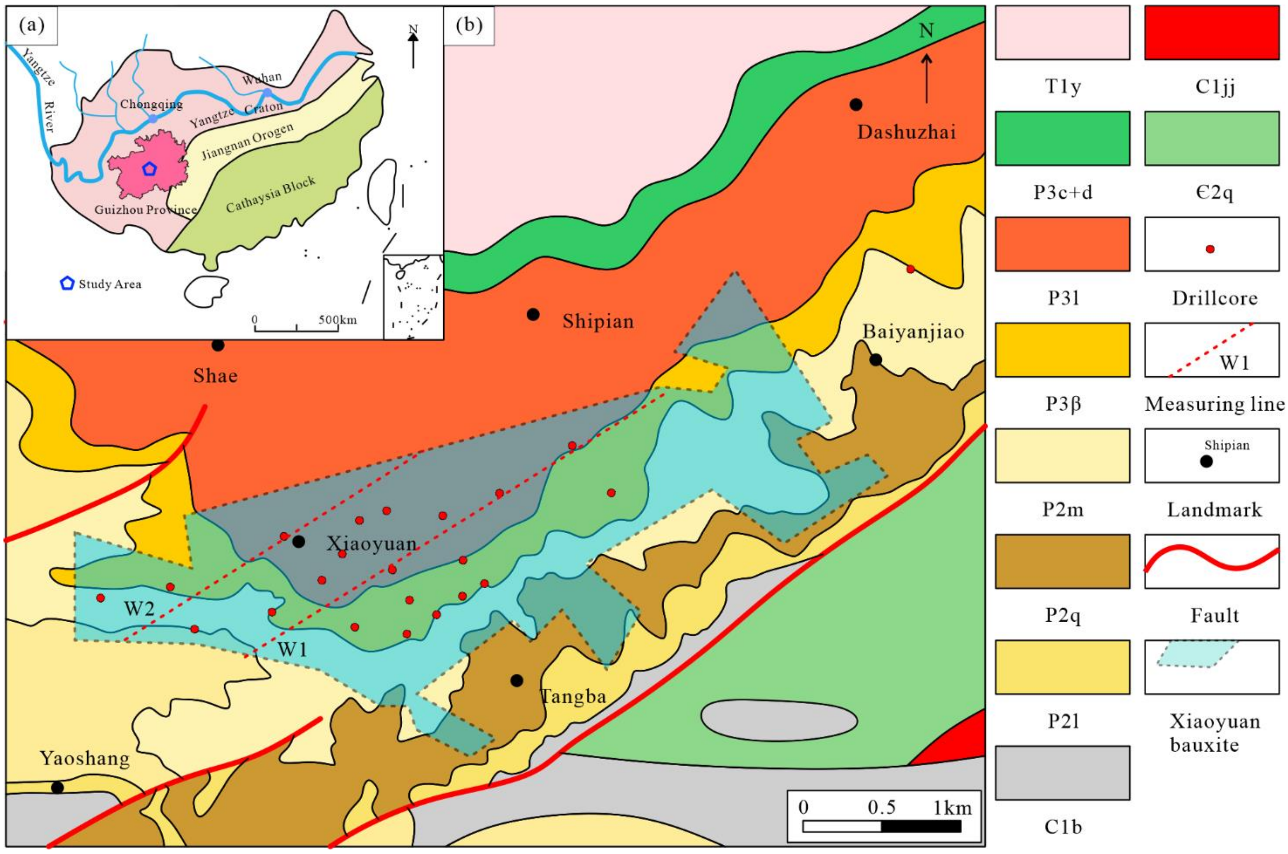

Figure 1. (**a**) Map of the South China Block showing the Yangtze Craton and the location of the study area in the Yangtze Craton (the map of the South China Block was modified from [21]); (**b**) regional geological map of the Xiaoyuan area bauxite ore field.

2.2. Deposit Geology

Bauxite in the Xiaoyuan area, a newly discovered bauxite deposit, belongs to the Xiuwen Qingzhen bauxite deposit in the middle of the central Guizhou uplift (Figure 1b). The reserves include 20 million tons of bauxite, 1.57 million tons of pyrite, and 4.44 million tons of hematite (115 Geological Party, Guizhou Bureau of Geology & Mineral Exploration, unpublished report, 2022). Stratigraphically, in ascending order, the rock units include the Cambrian Qingxudong Formation, the Lower Carboniferous Jiujialu Formation and Baizuo Formation, the Middle Permian Liangshan Formation, the Qixia Formation and Maokou Formation, the Emeishan Basalt Formation, Upper Permian Longtan Formation, the Changxing Formation, the Dalong Formation, the Lower Triassic Yelang Formation, the Anshun Formation, and the Quaternary Formation. The Qingxudong Formation is the basement of the Jiujialu Formation. It primarily consists of dolomitic carbonate rocks. It is in parallel and unconformable contact with the Jiujialu Formation. The Baizuo Formation, comprising dolomite and dolomitic limestone, overlays the Jiujialu Formation. In addition to its conformable contact with the Jiujialu Formation, the Baizuo Formation also exhibits parallel unconformity contact with the overlying Liangshan Formation of the Permian age. The thickness of the Jiujialu Formation ranges from a few meters to tens of meters. According to the lithological changes, the Jiujialu Formation in the study area is divided into three layers: the lower layer is composed of iron clay rock, the middle is bauxite, and the upper layer is composed of aluminous clay rock with rich pyrite nodules. The bauxite ores are dominated by clastic and compact ores.

3. Sampling and Analytical Methods

Controlled-source audio-frequency magnetotellurics (CSAMT) and drill core data were used to conduct stratum modeling. The relationship between the sedimentary environment and the element distribution in the study area was investigated by analyzing the geochemistry of the elements. Samples were obtained from 23 drill cores in the study area. A total of 48 bauxite ore samples were selected from 17 ore drill cores for the principal element analysis. One bauxite ore sample each was selected from Zk5123, Zk1519, Zk0305, and Zk0608 for the X-ray diffraction (XRD) mineral phase analysis. Twelve samples of Zk0305 were used as low-iron bauxite samples for the conventional analysis of trace elements and B elements. Finally, three samples from the top to the bottom of Zk5123 were used as high-iron bauxite samples for the conventional trace element analysis as a comparison.

3.1. Controlled-Source Audio-Frequency Magnetotellurics

The audio-magnetotelluric (AMT) data used in this study were provided by the 115 Geological Party. The 115 geological team employed the V8 multifunctional electrical instrument (Phoenix Geophysics, Toronto, Canada) for data acquisition. Two parallel measurement lines were established in the exploration area following the strike direction of the strata towards the northeast. Measuring line W1 consisted of 81 electrode points, and W2 comprised 61 electrode points. Subsequently, the data were preprocessed.

The data were processed using SSMT2000 and MTEditor software (that comes with the V8 multifunctional electrical instrument). SSMT2000 uses a file with the time-series data, a calibration file, and a file with the measurement data as input to generate a Fourier transform factor. It processes the data using reference point data with the Robust program and provides output data readable by MTPlot software. The output file contains the crosspower (a single-frequency overlay factor) for each frequency. MTEditor was used to read the output file of SSMT2000 and display the resistivity, phase curve, and crosspower to calculate the electromagnetic parameters of a specific frequency. The resistivity data and phase curve were edited in MTEditor, and the industrial standard EDI and PLT files were output. One-dimensional (Bostick, OCCAM) and two-dimensional RRI (Rapid Relax Inversion), NLCG (nonlinear conjugate gradient inversion) inversion models were used in the AMT inversion software [22–26]. Different inversion results were compared, and the optimum inversion results were selected based on geological data. Finally, Surfer 15 software (Golden Software, Golden, CO, USA) was used to create the apparent resistivity profile with kriging interpolation (Figure 2a,c).

3.2. Geological Modeling

After the deposition of the Jiujialu Formation, a series of tectonic movements occurred, albeit with minimal impact on the topography of the mining area [20,27]. It was during the Yanshanian orogeny that the central Guizhou area experienced intense folding and deformation, resulting in the current position of the mining area being on the limb of an anticline [20]. Consequently, the Xiaoyuan area is situated on an inclined plane, dipping to the northwest at an angle of 20°. The tilting of the strata has caused a significant vertical displacement of up to 400 meters, necessitating corrective measures to restore the paleogeography of sedimentary mineralization period.

In this study, Matlab programming was employed to establish the XYZ coordinate axis based on the coordinates extracted from the apparent resistivity inversion map and drill core data. A northeast direction (perpendicular to the stratigraphic dip) was assumed, parallel to the XY-plane axis in this coordinate system. Subsequently, the extracted coordinates were rotated clockwise by 20° around the axis and converted into new coordinates to compensate for the impact of the Yanshan movement on the strata in the region. Finally, kriging was used in Surfer 15 to establish the stratigraphic model using the converted coordinates.

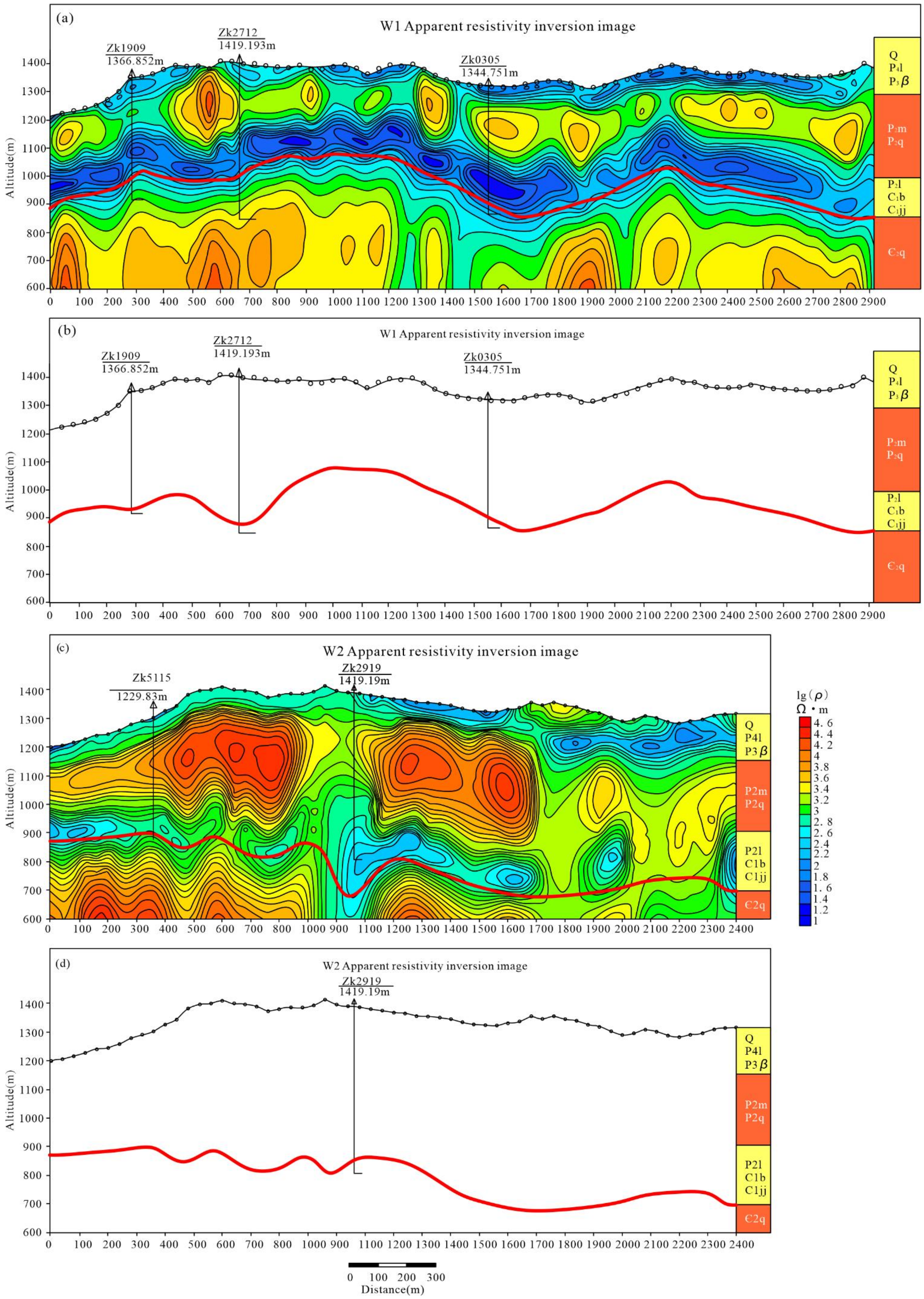

Figure 2. (**a**) Magnetotelluric sounding apparent resistivity profile inversion map for W1; (**b**) corrected curve of the Cambrian basement for W1; (**c**) magnetotelluric sounding apparent resistivity profile inversion map for W2; (**d**) corrected curve of the Cambrian basement for W2.

3.3. Analysis of the Major Elements

A major element analysis was performed on 48 bauxite ores samples from 17 drill cores and 12 samples from Zk0305 in the study area. Al_2O_3, SiO_2, Fe_2O_3, and TiO_2 were measured by X-ray fluorescence spectrometry. An NH_4NO_3 solution or $LiNO_3$ was used as a pre-oxidant, and a small amount of LiBr or NH_4I solution was added as a release agent. Subsequently, the sample was melted and cast into glass samples in an automatic fusion machine. In the final stage, the fluorescence X-ray intensities of various elements were measured using an X-ray fluorescence spectrometer. A calibration curve was established to correlate the observed X-ray intensities with the elemental concentrations. A calibration equation was used to correct the absorption enhancement effect between elements. The element contents were calculated from the calibration curve.

3.4. Analysis of Trace Elements

A trace element analysis was carried out with twelve samples of Zk0305 and three samples of Zk5123 at the ALS Minerals-ALS Chemex Laboratory (Guangzhou, China). The conventional trace elements were dissolved by four-acid digestion and analyzed by inductively coupled plasma atomic emission spectroscopy and mass spectrometry. After the samples had been digested with perchloric acid, nitric acid, hydrofluoric acid, and hydrochloric acid, the volume was fixed with dilute hydrochloric acid, and the sample was analyzed with an inductively coupled plasma emission spectrometer. If the contents of Bi, Hg, Mo, Ag, and W were high, it was necessary to dilute the sample and reanalyze it. After the spectral interference between the elements had been corrected, the final result was obtained. The B elements were analyzed separately. The sample was weighed and placed into a nickel crucible, and sodium hydroxide flux was added to the sample, which was thoroughly mixed and fused at a high temperature. The molten material was cooled and dissolved with deionized water to obtain a volume of 100 mL. An equal amount of HCl was added to the solution, mixed thoroughly, and analyzed by inductively coupled plasma mass spectrometry. The final analysis result was corrected by the spectral interference between the elements.

3.5. XRD

XRD was carried out in the Guiyang Science Compass Laboratory in Guizhou Province. The mineralogical compositions of the whole-rock powder samples were determined using a Rigaku Ultima IV X-ray powder diffractometer under the following operating conditions: a voltage of 40 kV, a current of 40 mA, a scanning speed of 5°/min, and 2-theta (°) ranges from 5° to 60°. The major mineral phases were identified from the XRD patterns using the ICDD PDF-2 database and Jade 6.0 software.

3.6. Mineralogical Analysis

Scanning electron microscopy (SEM) was conducted at the State Key Laboratory of Ore Deposit Geochemistry, Institute of Geochemistry, Chinese Academy of Sciences. The micro-mineralogical analysis was carried out using thermal field emission scanning electron microscopy (FE-SEM) (JSM-7800F). The working conditions were a 20 kV acceleration voltage, a 1.6 nA current, a 10 mm working distance, and a 1 μm beam diameter. A thin layer of carbon was sprayed onto the sheet prior to the SEM analysis. The petrological investigation was carried out using a Zeiss Axio Scope optical microscope at the School of Resources and Environmental Engineering, Guizhou University.

4. Results

4.1. Inversion Map of Apparent Resistivity

The two apparent resistivity inversion maps show low resistance, high resistance, low resistance, and high resistance from top to bottom (Figure 2). Strata with different lithologies show different resistivity characteristics. Besides the lithology, different porosities and water saturations cause resistivity anomalies [28]. The interpretation of the apparent resistivity map requires prior understanding of the lithologic characteristics of the study area [29]. We compared the resistivity results of different tests of the lithology of the exposed strata in the study area (Table S1). The resistivity of the Quaternary overburden on the surface of the study area is 78.59–197.27 Ω·m, that of the underlying Permian siltstone, clay rock, and basalt is 96.72–2374.42 Ω·m, and that of the limestone is 2696.79–6625.37 Ω·m. The resistivity of dolomite and limestone in the Carboniferous is 1435.23–2779.4 Ω·m, and that of the bauxite layer is 125.63–867.03 Ω·m; the resistivity of the Cambrian dolomite basement ranges from 2435.23 to 5779.4 Ω·m. The thicknesses of the strata in the study area were compared (the thickness of the Permian Liangshan Formation is 17–31 m, that of the Baizuo Formation is 50–80 m, and that of the Jiujialu Formation is 0–25 m). It is speculated that the second-lowest resistivity anomaly is the result of the joint action of the silty clay rock at the bottom of the Permian, the carbonate rock of the Carboniferous Baizuo Formation, and the aluminous rock series of the Jiujialu Formation. However, many factors affect underground formation resistivity, including lateral rock resistivity, karst caves, and fractures [28]. Therefore, the formation morphology needed to be adjusted based on the drill core data. The two electromagnetic sounding lines were corrected by data obtained from Zk3909, Zk2712, Zk0305, and Zk2919 at the corresponding positions. A more accurate Cambrian basement topography was obtained after the correction, and the information was converted into coordinate data for geological modeling.

4.2. Geological Model

Paleogeomorphology is the result of the combined actions of many geological processes and affects the sedimentation and mineralization of aluminous rock series [9]. Analyzing the paleo-geomorphological characteristics is critical for understanding the paleokarst and mineral layer features. Maps of the thickness of the ore layers (Figure 3a) and the Jiujialu Formation strata (Figure 3b) were created. Kriging in Surfer 15 software was used to establish a stratigraphic model (Figure 3c).

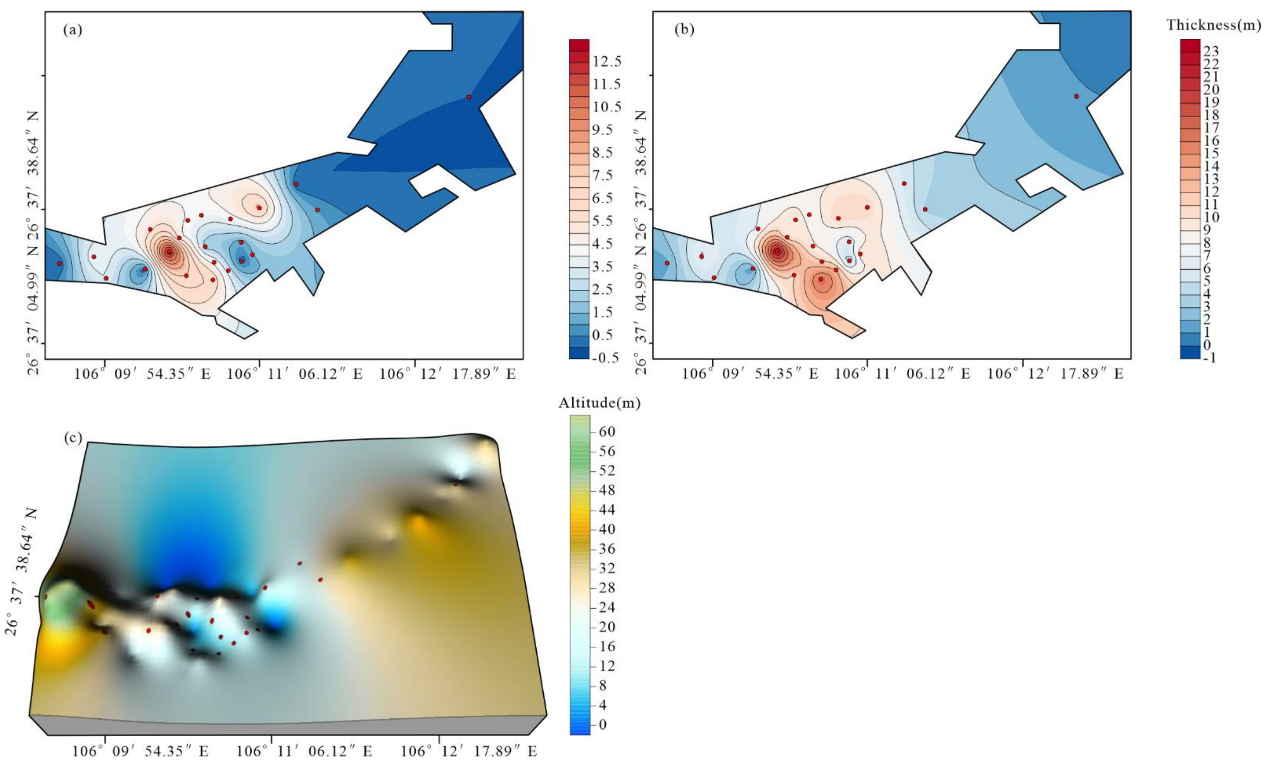

Figure 3. Geological modeling results of the Qingzhen Xiaoyuan bauxite deposit. (**a**) Thickness of the ore layer; (**b**) thickness of the aluminous rock series; (**c**) stratigraphic model of the Cambrian Qingxudong Formation.

4.3. Geological Characteristics and Distribution of Bauxite Deposits in the Study Area

Based on the geological modeling results derived from the geological data (Figure 4a,b), the study area has higher elevations in the eastern region and lower terrain in the central part. The Jiujialu Formation, which consists of an aluminous rock series, is deposited on a karst basement. Bauxite deposits primarily occur in three distinct karst depressions at different elevations (referred to as B1, B2, and B3).

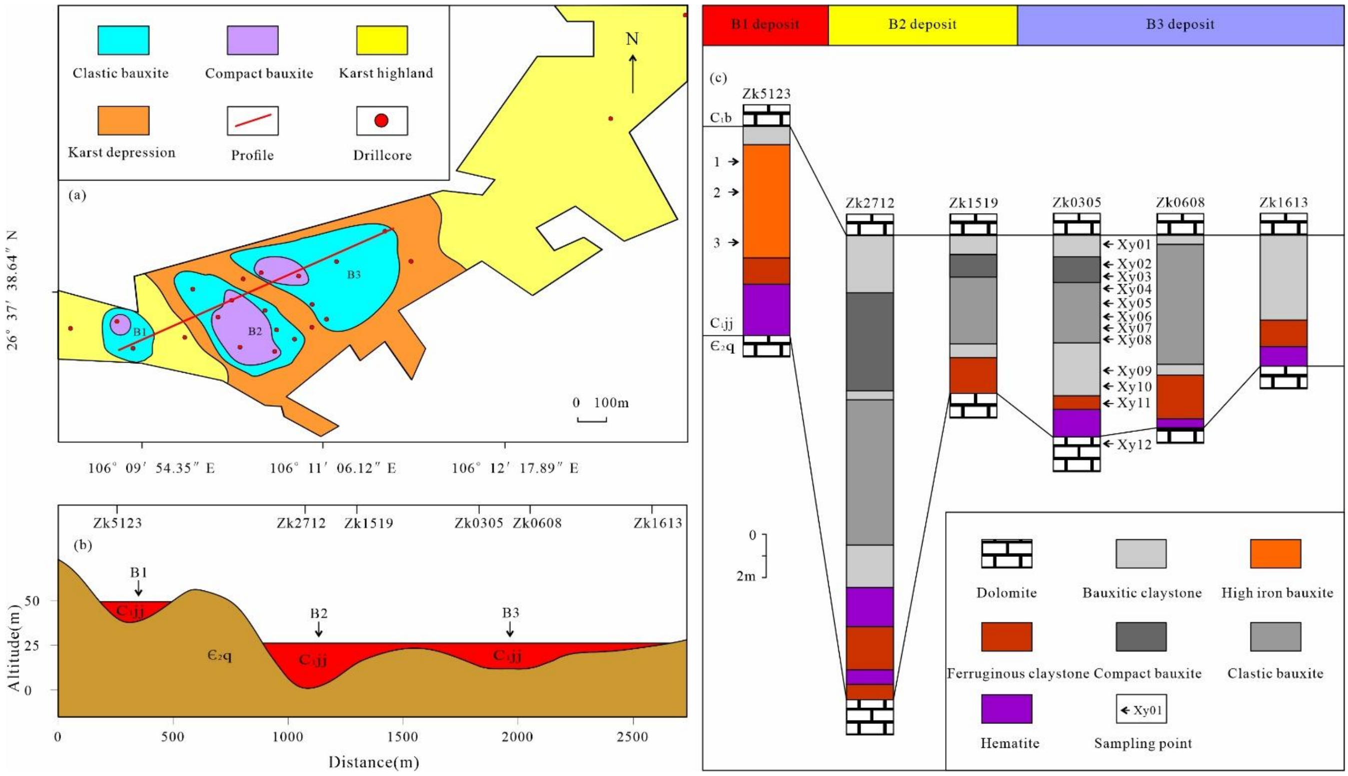

Figure 4. Karst topography map and drill core profile for the Xiaoyuan bauxite area. (**a**) Division of karst landforms in the study area; (**b**) cut profile; (**c**) drill cores on the cut profile.

The B1 deposit is situated in the western karst highlands and is characterized by red, low-grade bauxite with a high iron content. The bauxite ores in this deposit exhibit compact and clastic interbedded structures. The lower boundary of this deposit is approximately 40 m above the relative altitude, whereas the aluminous rock series thickness is about 10 m. The ore layer in the deposit has an approximate thickness of 5 m.

The B2 deposit consists of high-grade, dark gray bauxite. The majority of the bauxite ore in this deposit is clastic. In some drill cores in the central depression, a clastic structure is observed in the lower layer, while a compact structure is present in the upper layer. The B2 deposit extends across the western side of the central karst valley, with its bottom boundary at a relative altitude of 0 m. The aluminous rock series thickness measures approximately 25 m, whereas the ore layer reaches a thickness of 14.1 m.

Similarly, the B3 deposit shares similarities with the B2 deposit, featuring dark-gray, high-grade bauxite characterized by a clastic structure. It is distributed on the eastern side of the central karst valley. The bottom boundary of the B3 deposit is positioned at a relative elevation of 15 m. The thickness of the aluminous rock series is 10.86 m, and the ore layer has a thickness of 6.9 m.

The aluminous rock series in all three deposits exhibit a sequential structure of iron-rich claystone, bauxite, and aluminous claystone from bottom to top. However, it is noteworthy that these formations lack the occurrence of carbonaceous shale sandwiched between coal seams commonly found in the central Guizhou region [30,31].

In the Zk0305 sample, the top of the aluminum-rich claystone in the Jiujialu Formation is composed of bauxite and claystone, which are interbedded and have clastic, oolitic, and pellet textures. Moreover, abundant pyrite masses have entered fractures and aggregated along them, showing intrusive and conglomerate textures. The area of the pyrite masses decreases from the top to the bottom of the formation (Figure 5a). Pyrite has predominantly developed in white kaolin claystone and bauxite, exhibiting fine-grained textures (Figure 5b). The bauxite ore layer is under the claystone and consists of light-gray clastic and earthy bauxite in the upper part, intercalated with dark gray aluminous claystone without bedding (Figure 5c). The lower part of the ore layer consists of clastic bauxite with poorly sorted and sub-rounded particles. A distinct boundary can be observed between the clastic bauxite and the earthy bauxite in the upper layer (Figure 5d). The interbedding of green clay rock and clastic bauxite occurs below the bauxite ore layer. Pyrite aggregates can be seen in the clay rock (Figure 5e). The bottom aluminous claystone is interbedded with dark gray-black claystone and light gray claystone. A large number of pyrite veins are located along the interlayer fractures, exhibiting spherical, large granular and narrow, and coarse vein-like textures (Figure 5f). A ferric rock layer is located under the aluminous claystone, with a deep, gray-green chlorite layer on top. The cracks between the layers are filled by large amounts of pyrite (Figure 5g). A hematite layer occurs below and is interbedded with hematite and ferric claystone with good bedding development and large amounts of pyrite. The particle size decreases from the bottom to the top (Figure 5h). The bottom of the iron rock is interbedded with hematite and chlorite claystone, and the bedding is well-developed. The hematite exhibits a spheroid and oolitic structure locally, with the edge penetrating into the chlorite layer (Figure 5i).

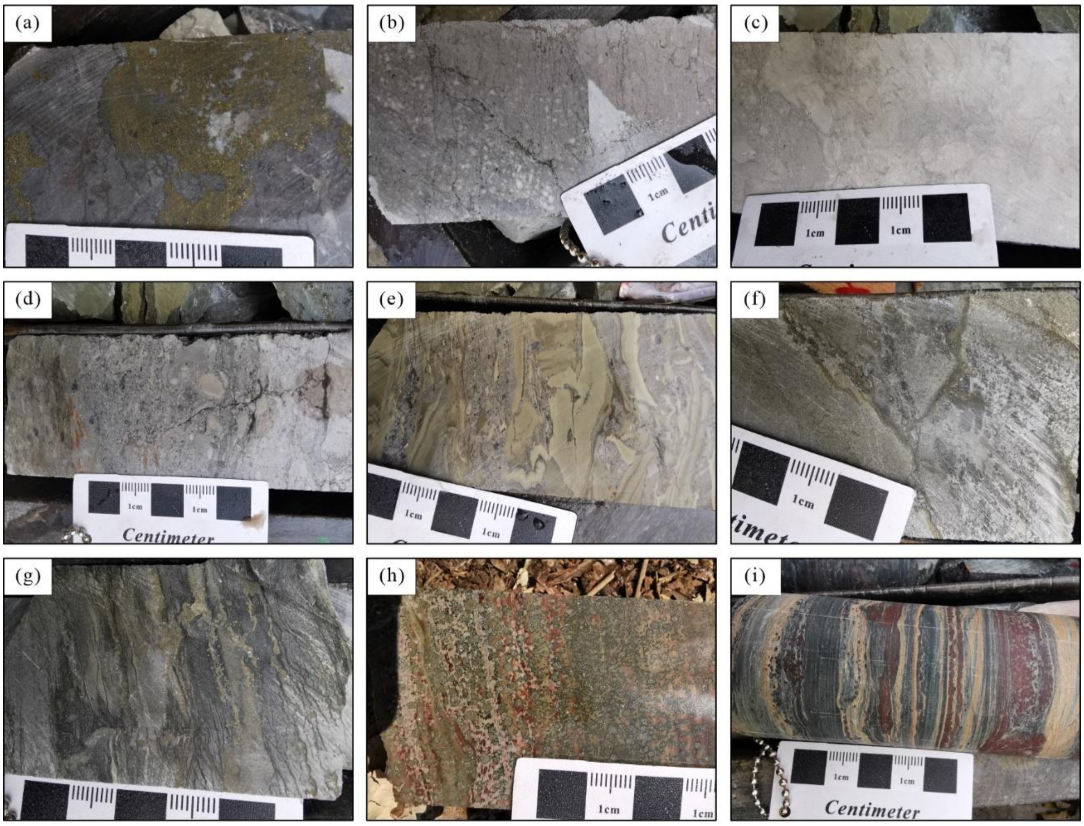

Figure 5. Photos of drillcore samples. (**a**) aluminous claystone and pyrite particles; (**b**) aluminous claystone and kaolinite; (**c**) clastic bauxite; (**d**) interbedded clastic bauxite and clay rock; (**e**) interbedded clay rock and clastic bauxite; (**f**) pyrite bands along the cracks between the bauxite beds; (**g**) pyrite bands along the cracks between chlorite clay beds; (**h**) oolitic hematite interbedded with chlorite claystone; (**i**) hematite interbedded with chlorite claystone.

4.4. Results of the Mineralogical Analysis of Karst Geomorphology

A mineralogical analysis of the bauxite ores from three bauxite deposits was conducted. An XRD analysis (Figure 6) was performed to determine the mineral phases. Subsequently, optical microscopy and SEM were used to analyze the mineral morphology and contact relationships.

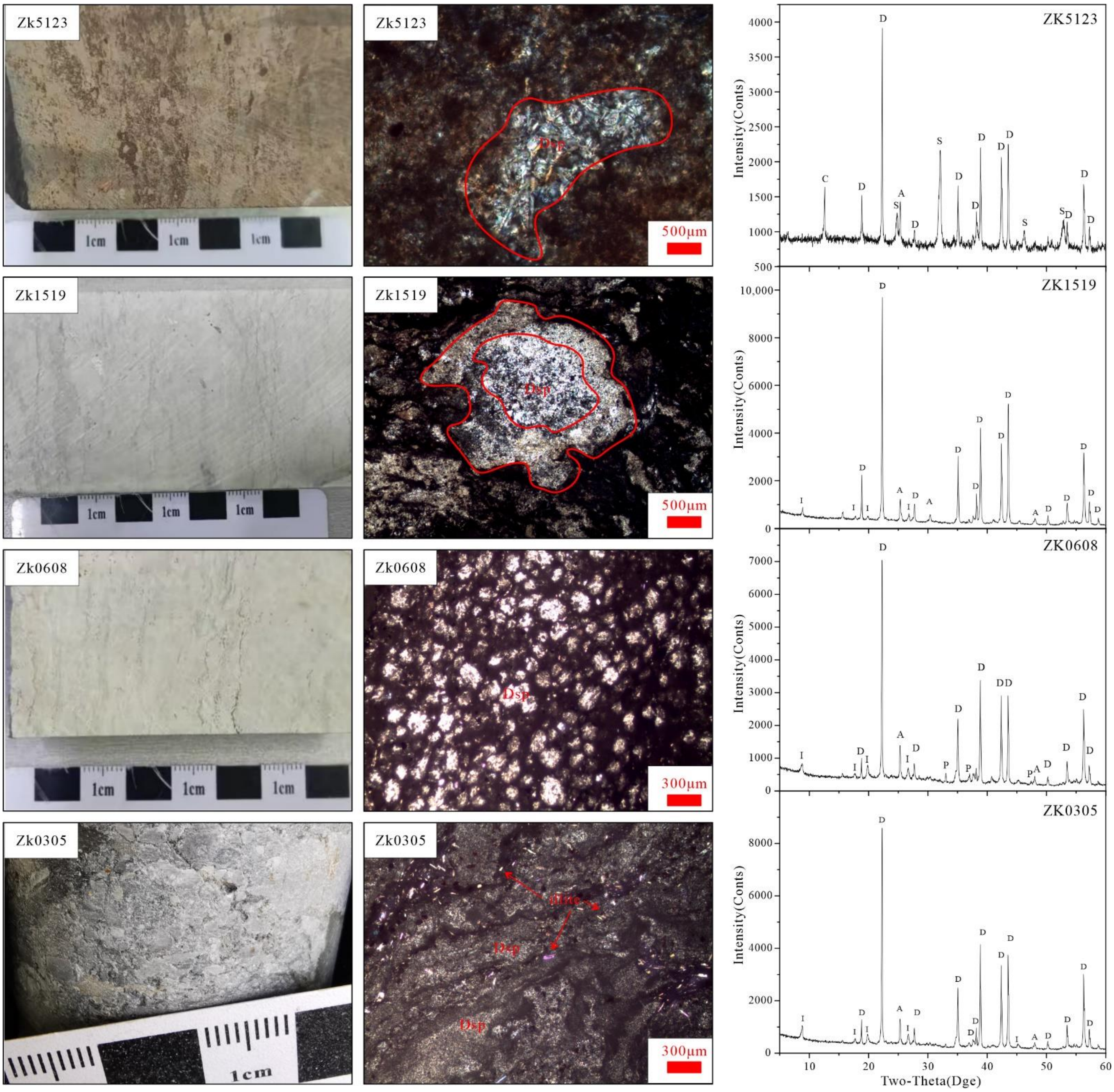

Figure 6. Mineral characteristics of the Qingzhen Xiaoyuan bauxite deposit. Zk5123 is high-iron bauxite, and Zk1519, Zk0608, and Zk0305 are low-iron, high-grade bauxite deposits; A = anatase, D & Dsp = diaspore, I = illite; P = pyrite; S = siderite; C = chlorite.

In deposit B1, samples were taken from Z5123, which is characterized by high-iron bauxite with a deep red color. The bauxite structure in this deposit is clastic. A microscopic examination revealed the presence of aphanite and columnar diaspore (Figure 6 Zk5123). The XRD mineral phase identification confirmed the presence of diaspore, chlorite, anatase, siderite, and other minerals in the bauxite. SEM revealed the presence of iron pisolites in the high-iron bauxite with a core of siderite (Figure 7a). The bauxite ore predominantly consists of diaspore, occurring as short columnar crystal aggregates with well-formed crystals. These diaspore crystals coexist with siderite and the diaspore crystals are surrounded by siderite (Figure 7b). Additionally, well-formed hematite crystals are found in certain locations, surrounded by siderite. (Figure 7b).

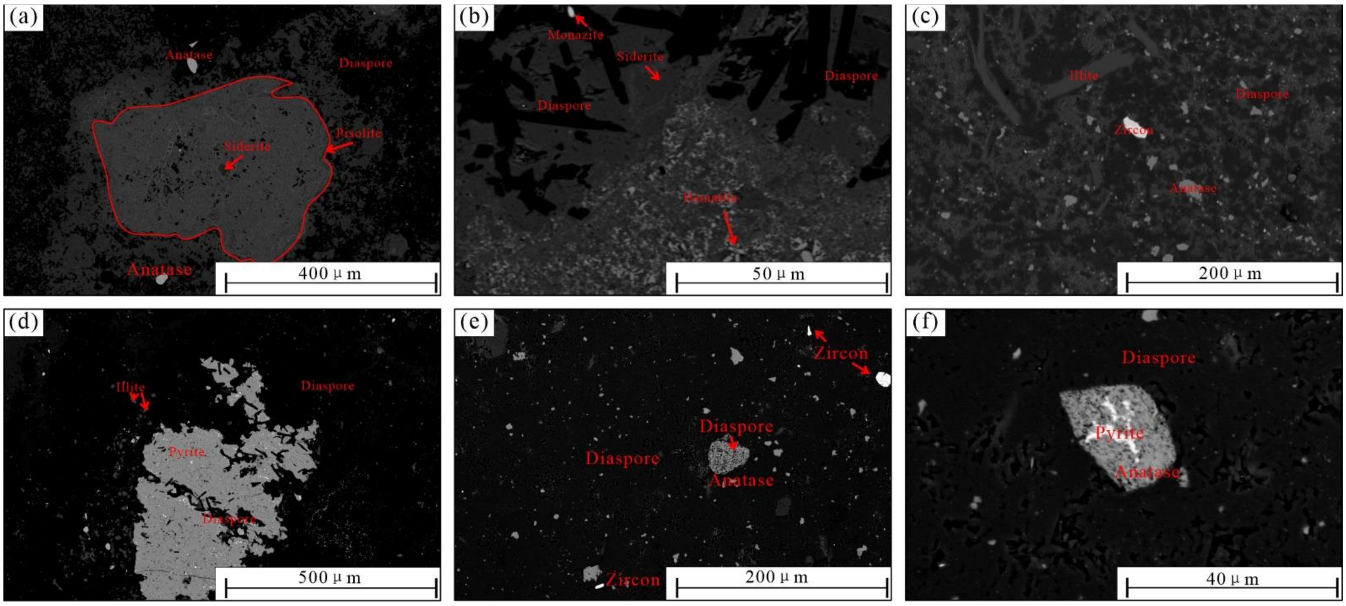

Figure 7. Backscattered SEM images of the samples showing the major minerals and their relationships: (**a**) iron pisolite; (**b**) hematite with a good crystalline form surrounding the siderite and diaspore aggregates; (**c**) diaspore and illite surrounding each other and some anatase and zircon; (**d**) pyrite surrounded by diaspore with a good crystalline structure; (**e**) anatase surrounded by diaspore; (**f**) anatase surrounded by pyrite and diaspore.

The sample from Zk1519 in the B2 deposit contains diaspore, illite, anatase, and other minerals. The bauxite ore has an earthy clastic structure. The microscopic analysis indicates that the large-grained, oolitic aggregate diaspore has formed zones according to the crystallization degree, and the crystallization degree inside is higher on the inside than on the outside (Figure 6 Zk1519). The SEM images show short columnar or cryptocrystalline diaspore and illite, anatase, and zircon (Figure 7c).

Two drill cores (Zk0305 and Zk0608) were selected for sampling in the B3 deposit. The bauxite ores show a grayish-white and dark-gray clastic soil structure. The XRD analysis indicates the presence of diaspore, illite, anatase, and pyrite. Microscopic analysis shows that the structure of the diaspore is cryptocrystalline with spheroidal aggregates and clay minerals. The SEM images show cryptocrystalline diaspore, illite, and pyrite with a good crystalline structure. Furthermore, widespread occurrences of mutual inclusions of diaspore, anatase, and pyrite are detected in the B2 and B3 deposits (Figure 7d–f).

4.5. Geochemical Characteristics of the Karst Geomorphology

4.5.1. Geochemical Characteristics of the Major Elements

The Zk5123 and Zk5115 drill cores in the B1 deposit are high-iron bauxite with Al_2O_3 contents of lower than 60% (44.4%–56.67%), an Al/Si ratio of 2.64–11.84, and a high Fe_2O_3 content (11.96%–23.86%). The contents of SiO_2 and TS vary substantially with ranges of 4.24%–18.22% and 0.09%–4.56%, respectively, whereas the TiO_2 content has a small range of 1.88%–2.57% (Table S2).

The bauxite in the B2 and B3 deposits is low-iron and high-grade bauxite. Zk0305, Zk0608, Zk0719, Zk1508, Zk1519, Zk1712, Zk2708, Zk2712, and Zk2919 have high Al_2O_3 contents (55.33%–77.85%), and the Al/Si ratio is 4.21–28.94. Moreover, samples with Al_2O_3

contents exceeding 70% occur in each drill core. The Al_2O_3 content of the bauxite ore in the Zk0504, Zk2304, and Zk2412 drill cores is medium (51.81–67.55), and the Al/Si ratio is 4.89–12.20. Samples with Al_2O_3 contents exceeding 60% can be observed in each drill core. The Al_2O_3 contents of Zk0506 and Zk1706 are lower (40.69–59.60), and the Al/Si ratio is 2.21–12.40. The Fe_2O_3 contents in these two deposits are low (0.30%–19.68%, with an average of 2.51). Only two ore samples (Zk0504 and Zk0506) show high-iron characteristics, with contents of 11.99% and 19.68%, respectively. The TiO_2 content varies considerably (1.60%–4.47%, with an average of 3.31%). A low sulfur content (<3%) is common in these three deposits, and only five samples (Zk0504, Zk1706, Zk2919, and Zk5115) have high sulfur contents (4.29%–8.71%).

Zk0305 is used as an example to describe the element distribution in a low-iron bauxite deposit. The Al_2O_3 content in the upper aluminous claystone is 30.97%, that in the lower bauxite deposit is 46.84%–71.62%, and that in the iron clay rock is 12.03%–25.13%. The Ti content does not vary significantly but is higher in the bauxite (0.96%–2.13%) than in the claystone (0.88%–0.68%). The Fe content is 9.83% in the top clay layer and 18.45–39.70 in the bottom clay layer, and the bauxite content is very low. The sulfur content in the bauxite layer is very low (0.03%–2.66%), but sulfur is enriched at the top of the aluminous claystone and the top of the ferric clay rock (7.49% and 17.55%, respectively). The aluminous rock series has low contents of mobile elements, such as Na, K, Ca, and Mg. The K content is higher than that of other mobile elements (0.76%–4.24%) and is the highest (4.34) in the aluminous claystone. The Na, Ca, and Mg contents in the bauxite layer are very low (<0.5%), but the Mg content is higher than the Ca content. The distribution of the major elements is more uniform in the high-iron bauxite deposit Zk5123, and there is no delamination. In addition to the high iron content, the layer has a relatively low K content (0.02%–0.1%) and a high Mg content (0.61%–0.65%).

4.5.2. Geochemical Characteristics of the Trace Elements

The results for the trace elements show that the majority of samples from the low-iron bauxite area represented by Zk0305 contain Ba, B, P, and Zr concentrations in excess of 100 ppm (Table S3). Bauxite is also rich in Cr (69–104 ppm, mean 85.8 ppm), Nb (26.5–82.1 ppm, mean 54.1ppm), and Ni (2.9–588 ppm, mean 124.7 ppm) (Table S3). The contents of As, Cu, Li, Ni, and Pb in the top aluminous claystone are significantly higher than those in the lower bauxite and ferric claystone, but the As, Ni, and Pb contents are highly enriched (64.40 ppm, 588 ppm, and 211 ppm, respectively). The B content is higher in the Jiujialu Formation (71–388 ppm) than in the bottom Qingxudong Formation dolostone (12 ppm). The Ba content is higher in the bauxite layers (840–1590 ppm) than in the ferric rocks (20–970 ppm) and the top aluminous claystone (70 ppm). The Cr content is higher in the upper (93–104 ppm) than in the lower bauxite layer (69–87 ppm). The contents of high field-strength elements (HFSEs) (Nb, Ta, Zr, and Hf), Th, and Ti are higher in the bauxite layer than in the top clay layer and the bottom iron layer. The P and Sr contents are lower in the upper bauxite layer than in the lower bauxite layer, and the P and Sr contents are highly enriched in the ferric rocks. The distribution trends of Rb, V, and Y are the same, and their contents increase from the upper bauxite layer to the lower bauxite layer and the ferric claystone. According to the total rare earth element (REE) content (39.58–859.55 ppm, average of 375.538 ppm), the bauxite in Xiaoyuan is enriched in REEs. The distribution of heavy REEs (HRREs) (La, Ce, Pr, Nd, Sm, Eu) is relatively uniform, whereas the light REEs (LRREs) (Gd, Tb, Dy, Ho, Er, Tm, Yb, Lu) are concentrated in the lower bauxite layer (273.29–810.99 ppm). Their contents are similar to that of the iron claystone at the bottom (195.14–236.37 ppm). The bauxite content in the upper layer (23.44–36.18 ppm) is similar to that of the dolomite in the Qingxudong Formation at the bottom (34.59 ppm). There are relatively stable negative Eu anomalies (0.43–0.76) in the entire aluminous rock series of the Jiujialu Formation, whereas the negative Eu anomalies in the dolomite of the bottom of the Qingxudong Formation are relatively weak (0.94). Stable positive Ce anomalies (1.15–1.53) occur in the upper bauxite layer, and significant changes in the Ce anomalies occur in the lower layer of the bauxite (0.75–1.42) and iron rocks (0.87–1.19). The chondrite-normalized REE plots indicate that the REE patterns of the upper bauxite and bauxite clay rocks are similar, with low $\sum$ REE contents (39.58–47.13 ppm, average 42.16 ppm), low $\sum$ LREE/$\sum$ HREE ratios (1.45–3.3), stable negative Eu anomalies (0.43–0.51), and positive Ce anomalies (1.15–1.52). The REE patterns of the lower layer bauxite and bauxite clay rocks are similar with high $\sum$ REE contents (412–671 ppm, average 575.58 ppm), high $\sum$ LREE/$\sum$ HREE ratios (12.87–21.55), stable negative Eu anomalies (0.55–0.76), and weakly positive Ce anomalies (0.75–1.41). The content of $\sum$ REE in the lower iron rock is low (224.9–285.1 ppm, average 251.17 ppm), and the $\sum$ LREE/$\sum$ HREE ratio is high (4.84–6.54). There are stable negative Eu anomalies (0.71–0.76) and weak positive Ce anomalies (0.87–1.19), and their REE patterns are similar to those of the lower bauxite layer. The dolomite of the Qingxudong Formation has a low $\sum$ REE content (53.22 ppm) and a high $\sum$ LREE/$\sum$ HREE ratio (1.85), with weak negative Eu anomalies (0.93) and positive Ce anomalies (1.23). Its REE pattern is similar to that of the upper bauxite layer.

The samples of the high-iron bauxite deposit represented by Zk5123 have a high iron contents (8.39%–11.5%) and low and stable Ba and Sr contents (30–60 ppm and 199.5–253 ppm, respectively), and the other elements' characteristics are similar to those of the lower low-iron bauxite. The REE content is higher in the high-iron bauxite (606.41–1485.23 ppm), and it is more enriched in LREE than in HREE. The REE pattern is similar to that of the lower-layer bauxite. Stable and positive Ce anomalies (1.11–1.6) and negative Eu anomalies (0.56–0.59) can be observed.

5. Discussion

5.1. Effect of the Karst Geomorphology on Mineral Facies

The B1 deposit predominantly consists of diaspore, siderite, anatase, and chlorite. The mineral assemblages are similar in the B2 and B3 deposits, consisting of diaspore, pyrite, illite, and anatase minerals.

Previous studies have indicated that the diaspore in the bauxite deposits of central Guizhou is primarily derived from gibbsite transformation [2]. However, recent research has revealed that the diaspore in karst bauxite deposits originated not only from metamorphic processes but also from simple crystallization processes [32–37]. Generally, diaspore in karst bauxite forms under supergene conditions in alkaline and reducing environments [11,34,38]. Similarly, anatase formation occurs under reducing conditions [5,33,37]. In contrast, gibbsite is more stable than diaspore and boehmite under supergene conditions [7,35]. Mineral phase transformation from gibbsite to boehmite and diaspore is common in karst bauxite due to the combined effects of tectonic stress from later folding, burial metamorphism from overlying rock pressure, and hydrothermal processes [2,39].

The bauxite in the B1 deposit in the study area has a short columnar structure with a good crystal shape, indicating that it was likely derived from the transformation of gibbsite formed during the weathering of ancient laterite. The heat required in this process was provided by the later tectonism or geothermal gradient [40]. The bauxite layer's mineral assemblage mostly comprises diaspore, siderite, anatase, and chlorite, indicating a reductive metallogenic environment [38]. Siderite exists as a matrix surrounded by anatase, indicating these minerals were formed by direct crystallization from water bodies in weakly alkaline and weakly reductive environments [5,33,34]. In addition, the hematite with a good crystal shape surrounding the siderite and diaspore (Figure 7b) indicates that the ore sample was subjected to oxidant modification in the later ore-forming period and to surface thinning caused by humic acid secreted by plant roots or weathering in the later period [7,34,41].

The B2 and B3 deposits are dark-gray, low-iron and high-grade bauxite deposits. The mineral assemblage of diaspore-pyrite-illite-anatase indicates a weak acid oxidation to a weak alkaline reduction metallogenic environment [42]. A cryptocrystalline diaspore ring can be observed around the oolitic diaspore (Figure 6 Zk1519), indicating that the diaspore continued to form after deposition. Spherical and oolitic granular diaspore is more likely to inherit the gibbsite shape and be affected by the subsequent metamorphism [16]. Cryptocrystalline diaspore is formed by super-crystallization or kaolinite desilication [33,34,37,43]. In addition, the B2 and B3 mining areas lack boehmite and gibbsite, suggesting the area suffered intense late mineralization, and the aluminous minerals were completely transformed into diaspore [16,33,34,38,40]. Recrystallization in diaspore may be the recrystallization product of a subsequent burial [44]. Finally, anatase, diaspore, and pyrite surround each other, indicating that anatase was inherited from the weathered parent rock and formed due to supergene crystallization [33,34].

5.2. Effect of Karst Geomorphology on the Element Distribution

5.2.1. Horizontal Element Distribution

We performed kriging to create a contour map of the element content of the bauxite ore in the drill cores (Figure 8).

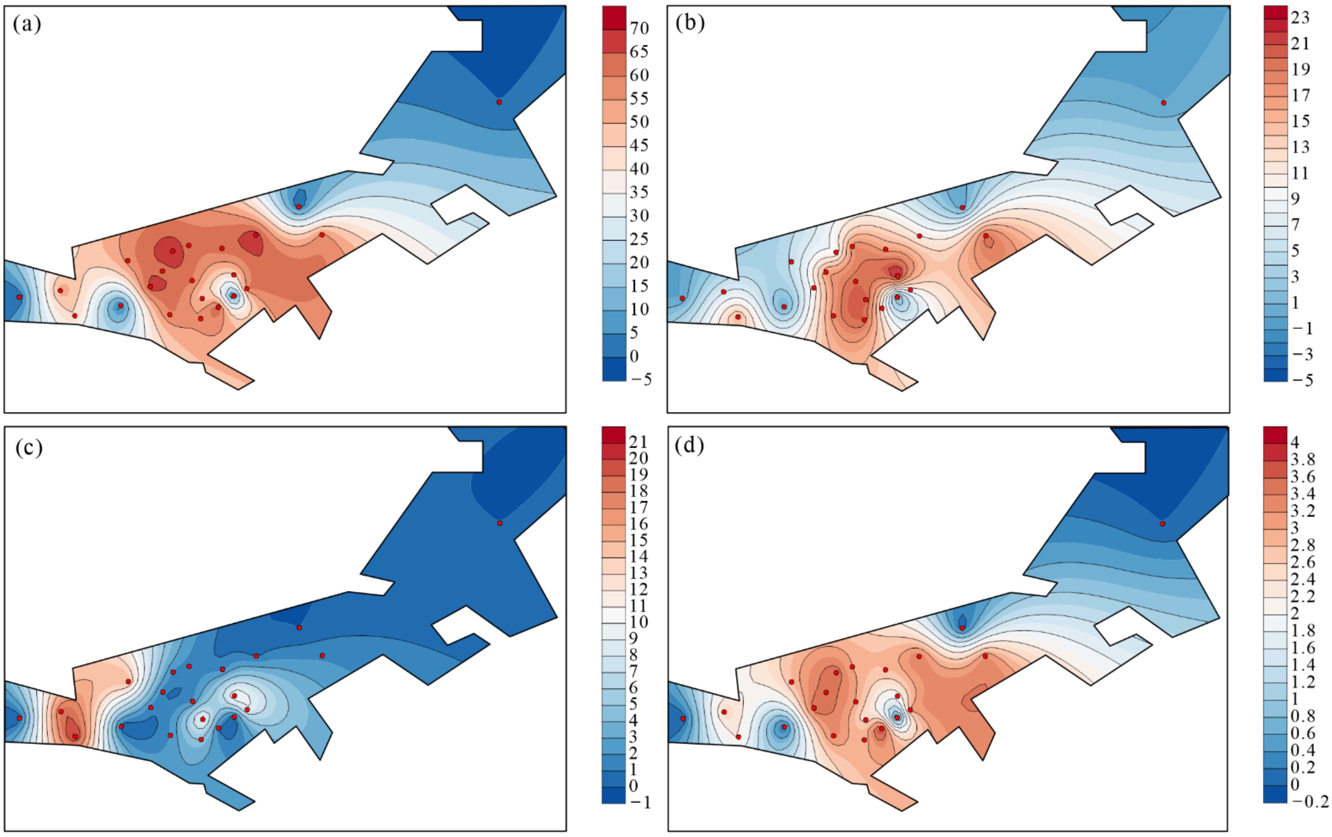

Figure 8. Distribution of major elements in Xiaoyuan bauxite in Qingzhen. (**a**): Al_2O_3; (**b**): SiO_2; (**c**): Fe_2O_3; (**d**): TiO_2.

The Al_2O_3 content is low in the B1 area (44%–53%) and high in the B2 and B3 areas (57%–69%). It is higher in the center of the karst depression than in the surrounding area, i.e., the deeper the karst depression, the higher the content. The distribution of the SiO_2 content has the opposite trend to that of the Al_2O_3 content, i.e., the deeper the karst depression, the lower the content. The content distribution of TiO_2 is highly similar to that of Al_2O_3. Previous studies showed that bauxite was deposited in negative terrain [7,9,45]. The karst depression in the study area serves as a sink area for sediments, and almost all negative terrain areas have bauxite. Horizontally, the compact bauxite is primarily found in the center (Figure 4a), consistent with high-grade bauxite (Figure 8a), whereas the clastic bauxite surrounds these areas (Figure 4a), but its grade is lower (Figure 8b). Some researchers believe that the bauxite morphology is related to the strength of the hydrodynamic forces during sedimentation. Detrital bauxite predominantly forms in areas with strong hydrodynamic forces and unstable water bodies, whereas compact bauxite forms in deep karst areas with weak hydrodynamic forces and stable water bodies [9,14].

The distribution of clastic bauxite in the lower part and compact bauxite in the upper part of the study area suggest that highly weathered paleolaterite was transported to the karst depression, forming clastic deposits under strong hydrodynamic forces during the deposition. As the detrital material was depleted, the source rock located in high erosion areas was weathered and transported as fine particles to the remaining locations in the karst depression, forming fine-grained to compact bauxite ore [14]. However, since there is no significant difference in the Al_2O_3 content between the clastic bauxite and the compact bauxite in this study, the ore morphology inherited from the deposition period cannot be determined by the Al_2O_3 content. This finding indicates that the transformation of Al-bearing minerals can affect the Al_2O_3 distribution in the bauxite horizon during the development and maturation of bauxite. The Al_2O_3 content in the depression center indicates that Al-containing substances migrated to the depression center in solution or as colloids during weathering and leaching.

The Fe_2O_3 content is high in the B1 deposit (18%–20%), low in the B2 and B3 deposits (8% on average), and higher around the karst uplift than in the center of the karst depressions. One possible explanation for the difference in the Fe_2O_3 content is that different formation periods of bauxite resulted in different degrees of iron removal [46]. Cheng et al. believed that high-iron bauxite was more likely to form in the deep part of the depression, and iron was directly precipitated from the water medium [12]. Siderite forms in a reduction environment, and hematite forms in an oxidation environment. Reference [47] analyzed the distribution of high-iron, low-grade bauxite and low-iron, high-grade bauxite in a large region and found that bauxite closer to the provenance area was more likely to have a high iron content. The drill core profiles in the study area revealed the presence of iron clay rocks beneath the bauxite layer. The deposition period of the iron clay strata is believed to be when the initial laterite was deposited in the soil-forming stage [48]. Fe ions dissociate under slightly acidic conditions and deposited in karst depressions, indicating that karst depressions form when the iron clay beds are deposited. The topographic differences between karst depressions may be attributed to different weathering levels of the carbonate basement before deposition. Under similar climatic and erosion conditions, chemical weathering often determines the weathering rate of carbonate rock, and physical weathering determines the final karst morphology [49]. Local crustal uplift occurred during the diagenetic and metallogenic period of the bauxite layer. The removal of Fe from the bauxite layer is related to microbial action and seawater intrusion [36,38,43,50,51]. Since the bauxite in this area is located in areas with high terrain and was not affected by seawater transformation during the deposition period, it was mainly influenced by continental deposition in addition to the influence of the paleokarst landform. The Fe_2O_3 content in the bauxite layer is relatively high around the karst uplift or in the karst highland, indicating that the initial bauxite material deposited in these areas provided iron-rich materials due to their proximity to the source area.

In summary, the distribution of the major elements and their correlation indicates that the migration of Al_2O_3, TiO_2, and SiO_2 occurred during the same process during element migration, with Al_2O_3 and TiO_2 in the retention phase and SiO_2 in the removal phase [16]. The Fe distribution suggests that there was no removal and retention relationship between Fe and Al during the migration process [17].

5.2.2. Vertical Element Distribution

The vertical element distribution in the study area is described using Zk0305 as an example. Zk0305 is located in the B3 deposit, and its stratigraphic lithology is complete, reflecting the element migration and transformation of the aluminous rock series from deposition to mineralization. The Al and Si contents in the aluminous rock series are used as a classification index. The section can be divided into the top bauxite stratum (Xy1), lower bauxite stratum (Xy3-8), and bottom iron clay stratum (Xy9-11). The top bauxite layer is thought to have been formed by re-silicification caused by humic acid during late diagenesis [4]. The interbedding of the clastic and compact structures and the inclusion of a clay rock mass in the central bauxite layer show the alternations of the hydrodynamic transport strength and rapid accumulation [14]. Aluminous claystone with a layered structure occurs at the bottom. The reason for this is that clay rock, a strong weathering surface of the source area, is preferentially transported and deposited at the bottom. As a result, the Al_2O_3 content of this layer is lower than that of the upper bauxite layer.

The distribution of Li, P, Sr, Y, HFSE, and REEs exhibits significant zoning, and the differentiation of these elements reflects changes in the weathering degree, sedimentary environment, or source [16,52–54]. Therefore, the aluminous rock series can be further divided into upper-layer bauxite (including the bauxite layer and bauxite clay layer, Xy1-3), the lower-layer bauxite (including the bauxite layer and bauxite clay layer, Xy4-8), and the iron rock at the bottom (Xy9-11). The P and Sr contents are low in the upper-layer bauxite, high in the lower-layer bauxite, and very high in the iron rock at the bottom. The Y content is lower in the upper-layer bauxite than in the lower-layer bauxite and lower in the bauxite layer than in the iron rock. The Li content shows that the upper and lower bauxite layers have undergone a process that reduced the Li content from high to low. The HFSE content in the bauxite ore is significantly enriched compared to the bauxite and iron clay layers. Zr and Hf are enriched in zircon, and Nb, Ta, and Ti are enriched in anatase and other titanium-bearing minerals [55]. The increases in the contents of these elements from top to bottom reflect the enrichment characteristics of these weathering-resistant minerals at the bottom.

The distribution pattern of REEs is often inherited from the weathered parent rock because the migration ability of REEs is limited during the weathering process [56]. The REEs in the bauxite mainly occur in REE-bearing phosphate minerals (monazite and phosphorite), hematite, and anatase [5]. Numerous studies have shown that REEs migrate and fractionate during epigenetic weathering, soil formation, and depositional diagenesis [53,57–62]. The LREE and HREE contents in the bauxite layer show an increasing trend from top to bottom (Figure 9). They are primarily enriched in the lower bauxite layer, indicating that the REEs (especially LREEs) in the upper bauxite layer were leached during bauxite mineralization due to strong chemical weathering and migrated downward with the leaching solution [53,63]. In addition, the bauxite layer exhibits a weakening of the Ce positive anomaly from top to bottom, suggesting that the layer was once in an acidic and oxidizing environment and suffered from strong leaching [30,53,62,64].

The negative Eu anomaly observed in the study area is indicative of intense weathering and is commonly used in bauxite studies to infer the provenance of the deposits [3,33,53,61,62,65]. The presence of a negative Eu outlier (0.43–0.76) in the study area falls within the range typically associated with felsic igneous rocks and upper continental crust materials. This result suggests that the provenance of the bauxite in the study area is a mixture of igneous rocks and upper continental crust materials [3,33,65]. Further evidence comes from U-Pb isotope dating of detrital zircons from the Maochang bauxite deposit in the Qingzhen area. This dating indicates that the primary source of the early Carboniferous bauxite in the Qingzhen area can be traced back to Mesoproterozoic felsic volcanic rocks and intrusive rocks that crystallized around 800 million years ago in the Panxi Hannan arc on the western edge of the Yangtze Plateau [40]. The felsic volcanic and intrusive rocks underwent multiple cycles of sedimentation, eventually forming Cambrian-Silurian sedimentary strata in the central and western Yangtze Plate. These sedimentary strata served as the ultimate material source for the development of early Carboniferous bauxite deposits in central Guizhou [40,66].

The correlation analysis showed that elements with moderate to strong correlations with Al_2O_3 are B, Ba, Th, LREEs, and HFSE, and the element with a strong correlation with SiO_2 is Li (Figure 10). B, Ba, Th, and LREE are HFSEs or elements that are positively correlated with Ti. Elements with positive correlations to P include Sr and HREEs, and Sr has a stronger correlation with P than the HREEs (Figure 9). The elements with positive correlations with Al_2O_3, Ti, and HFSEs are similar, indicating that the transfer of these elements during bauxite formation was caused by the same processes [52,62], likely weathering and leaching. The retention and formation of diaspore, zircon, and anatase caused the downward enrichment of these elements [16,55]. The strong positive correlation with SiO_2 indicates that these elements were easily removed during the mineralization of bauxite. B, which is strongly mobile in bauxite, is mostly adsorbed by the diaspore and clay in an ionic state [67,68]. The correlation analysis conducted on B, Al_2O_3, and SiO_2 indicates a significant positive correlation between B and Al_2O_3(Figure 10). Conversely, a weak negative correlation was observed between B and SiO_2. These findings suggest that B may have been preferentially adsorbed by diaspore. The adsorption of B depends on the pH; with pH < 7, some B may be released from the clay and absorbed by the aqueous aluminum oxide, since the latter has a strong adsorption capacity in slightly acidic conditions [69]. Franceschelli et al. (1998) reported a boron-rich bauxite deposit in Italy and attributed the boron enrichment to hydrothermal superposition [67]. Wang et al. (2012) reported B-rich bauxite in the Songqi area, southwest of Henan Province, and stated that B enrichment in bauxite often indicates that the bauxite is close to the B-rich source area [68]. The B content in the two B-rich areas exceeded 1000 ppm. However, no hot water transformation was observed in the Jiujialu formation, and the element test results showed that the B content in the dolomite basement was only 12 ppm, indicating that the provenance area did not have a high B content. Therefore, B likely has an external origin; it occurs in large quantities in seawater [70]. Therefore, the B in the bauxite in the study area may have come from seawater.

Since we did not obtain a complete set of samples for Zk5123, the results are only used as a reference for comparison with the low-iron bauxite. High-iron bauxite does not exhibit layers in the vertical direction, and its distribution characteristics of As, Cr, Cu, Ga, Ni, Pb, Sc, V, Y, Zr, and HFSE are similar to those of the low-iron bauxite. The distribution characteristics of P, Sr, and Th are similar to those of the low-iron bauxite in the lower layer. The REE distribution and Eu outliers are also similar to those of low-iron bauxite in the lower layer, indicating that their provenance may be the same. The Ba content in the three samples at different layers is much lower than that of the low-iron bauxite. Some studies have used the Sr/Ba ratio to assess the sedimentary environment because Ba and Sr are more likely to originate from seawater [52,71], and Sr has greater fluidity and is more prone to precipitation. However, bauxite generally suffers from strong chemical weathering and multi-stage leaching during its formation [72], causing changes in the contents of sensitive elements used to trace the sedimentary environment in bauxite. Thus, multiple or incorrect conclusions can be drawn using these sensitive elements to deduce the ore-forming environment of bauxite. The correlation analysis results indicate that the differences in the Sr and Ba contents may have been the results of different geological processes. Thus, it is not possible to assess the sedimentary environment based solely on the Sr and Ba ratio. As a strong mobile element, Sr is easily moved during weathering and leaching. Therefore, it should not be used to evaluate the sedimentary environment in areas with strong weathering and leaching. However, the Sr content is lower than that inherited from proto-rocks or seawater during the sedimentary period, and the correlation analysis shows that the Sr occurrence may be controlled by phosphate [73]. Ba is also a sensitive element in sedimentary environments and was possibly sourced from weathered parent rocks and seawater depositions [74]. However, regardless of the source, the high enrichment of Ba indicates that the area may have undergone strong seawater modifications and that weathering and leaching preserved it. The high Sr content of high-iron bauxite may have been inherited from weathered parent rocks and phosphate, whereas the low Ba content may indicate a lack of seawater participation in the transformation of the area, suggesting that it was formed by terrestrial sedimentation.

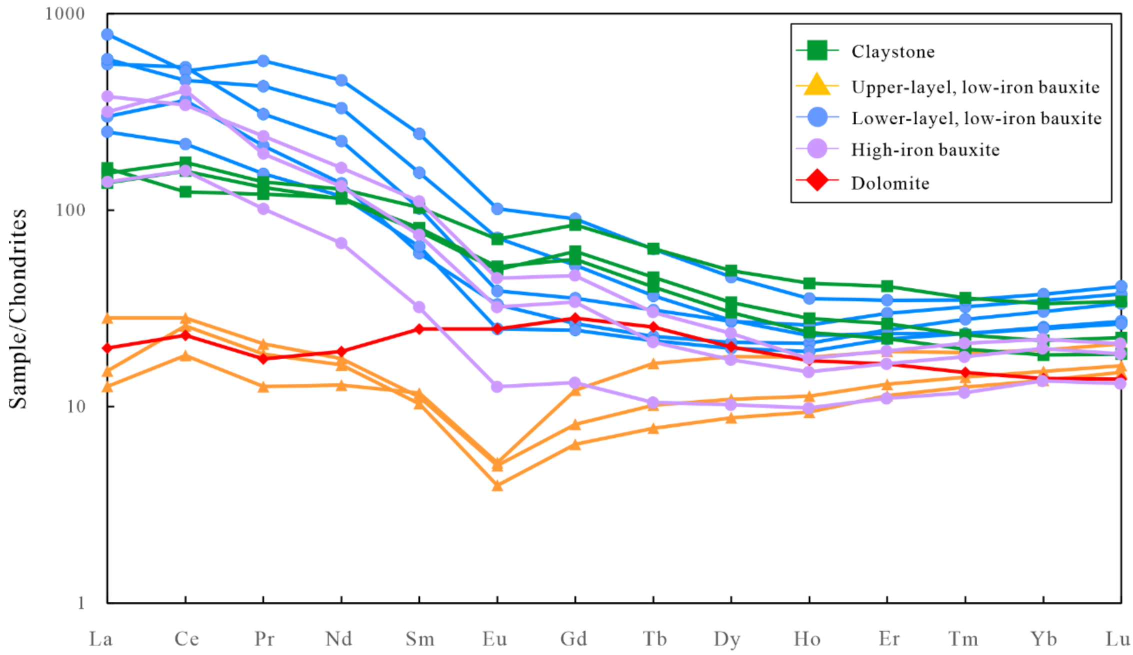

Figure 9. Chondrite-normalized REE patterns of samples from the Xiaoyuan bauxite deposit and the underlying Qingxudong Formation bedrocks (normalized values from [75]).

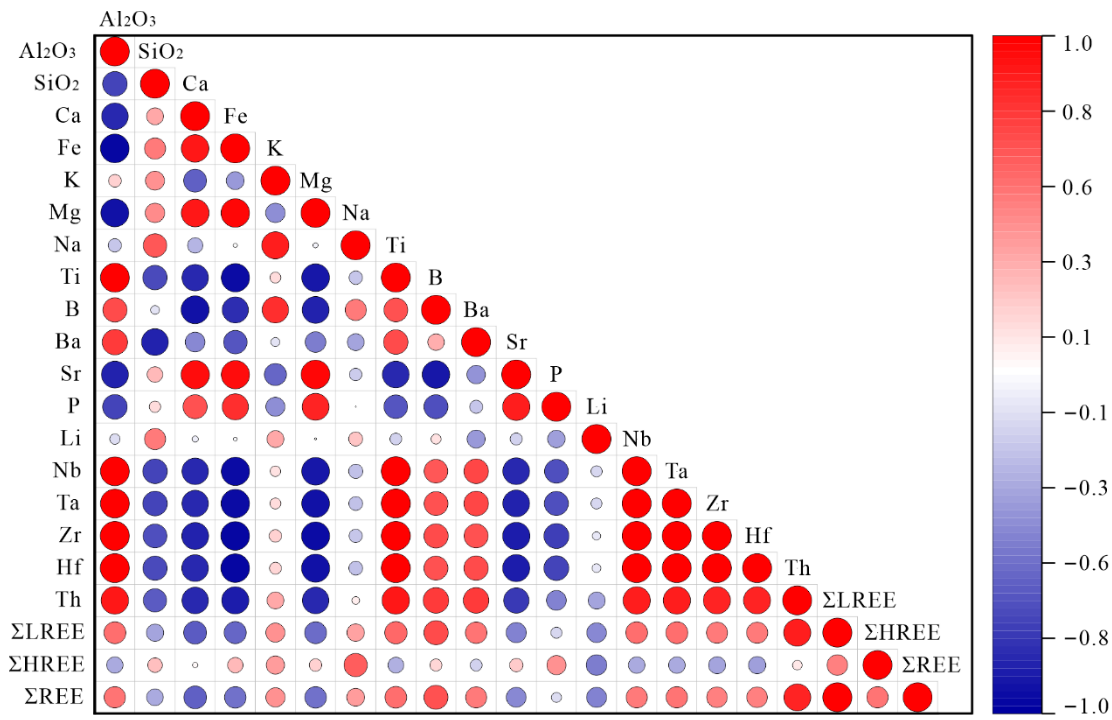

Figure 10. Correlation coefficients (Pearson's r) for elements in the Xiaoyuan bauxite deposit, central Guizhou Province.

5.3. Ore-Forming Process of Bauxite

Different genetic models of karst high-iron bauxite and low-iron bauxite are proposed based on the geological model, geochemical data, and mineral facies analysis conducted in this study, as well as previous studies on the metallogenic model of bauxite [1,2,16] (Figure 11).

In the late Ordovician, the central Guizhou region underwent Duyun movement and uplift to form the central Guizhou ancient land. After weathering and erosion, a set of marine carbonate rocks deposited since the late Cambrian formed a quasi-karst (or quasi-plain) ancient landform at the end of the Devonian [1]. Due to the drift of the South China Plate away from the equator near the end of the Devonian, the erosion level decreased, and the climate became hot and humid. The dissolution and erosion of the paleoenvironment intensified, forming karst landforms of various sizes and shapes [1]. Due to intense laterization, large amounts of crust material developed due to lateritic weathering and accumulated on the highlands surrounding these karst landforms. These materials were formed by laterization of the underlying Cambrian carbonate rock interbedded with silty rocks [1,43].

During the early stage of the Viséan, the rising sea level in southern China caused the karst depressions in the study area to be invaded by seawater, forming lagoons of various sizes. High rainfall caused by marine transgression formed shallow lakes in the karst depressions at higher elevations. Leaching occurred due to atmospheric precipitation and surface runoff. The fine clay minerals and complex amorphous gels of Al, Si, and Fe in the ancient lateritic weathering crust materials accumulated on the highlands surrounding the karst depressions were transported to nearby shallow lagoons under the protection of humic acid [76], forming the ironstone layer in the iron-stone–bauxite–claystone structure of the Jiujialu Formation.

As a result of further transgression from south to north in the South China Sea, the ancient weathered crust laterite materials accumulated on the highlands around the karst depression were submerged by sea water and moved to the adjacent karst depression, forming sediments that were transported by tides during the transgression and by seasonal floods generated by rainstorm [77]. Crystallization of diaspore, anatase, and chlorite occurred during this period owing to the weak alkaline and weak reducing environment provided by the carbonate basement and seawater intrusion. During the ebbing of the tide, the bauxite deposit was exposed to oxidation and seepage, causing a phase change from aluminosilicate mineral $\rightarrow$ clay mineral $\rightarrow$ aluminous mineral and the separation and removal of Fe due to leaching [36,43]. At this point, the karst depression situated in the west of the study area remained unaffected by the transgression because of its high elevation. Thus, continental lake deposits formed due to surface runoff from rainstorms and floods, ultimately forming continental bauxite. Surface runoff transported the weathering crust material of ancient laterite into the depression, forming the initial bauxite deposit. After rapid accumulation, the lower-layer bauxite was in a reducing environment, forming siderite, diaspore, pyrite, and anatase.

The Jiujialu Formation bauxite was deposited in a closed lagoon basin until a large-scale regression occurred in the middle stage of the Viséan, transforming the lagoon into saline, alkali land with high salinity due to evaporation. Subsequently, the salinity levels decreased due to precipitation and surface runoff, and the area evolved into a swamp covered by early Carboniferous flora [4,31]. As the plants grew, humic acid was generated and deposited in the upper part of the Jiujialu Formation due to atmospheric precipitation and surface runoff, resulting in a weakly acidic environment. These conditions slowed or stopped the bauxite mineralization in the upper part of the Jiujialu Formation. Desilicification also occurred, forming numerous clay minerals, such as kaolinite and illite, and the bauxite clay layer in the upper part of the aluminous rock series of the Jiujialu Formation.

The central area of Guizhou experienced the largest-scale marine transgression in the Carboniferous until the Serpukhovian, and the Baizuo Formation carbonate rocks were deposited on the aluminous rocks in the Jiujialu Formation. After the deposition of the Jiujialu Formation was completed, the gibbsite in the aluminous rock series was transformed into diaspore due to the pressure of the overlying rock, metamorphism, and the combination of the subsequent tectonic stress and hydrothermal action [1,2,11,72].

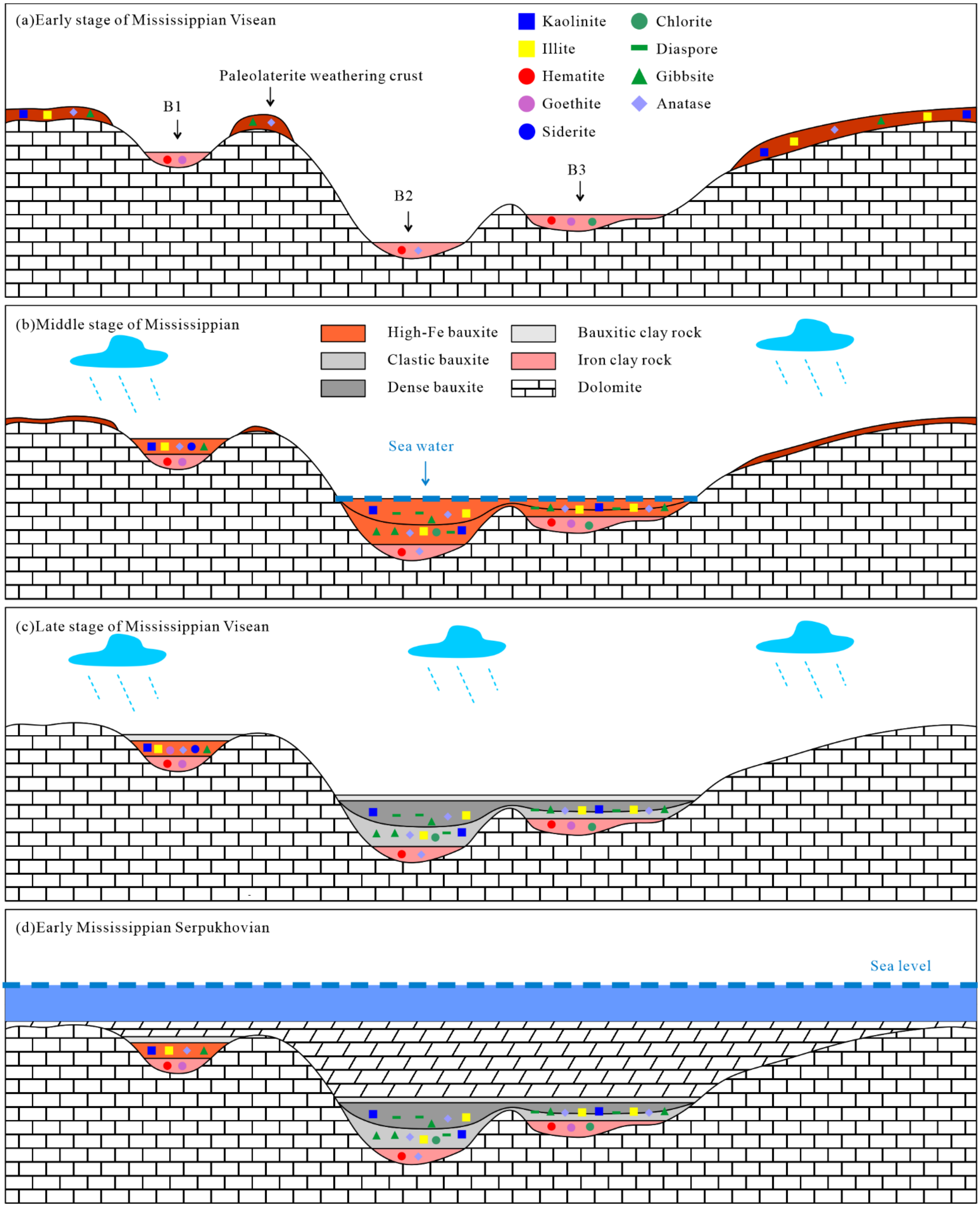

Figure 11. Ore-forming process of the Carboniferous karstic bauxite deposits in the Xiaoyuan area (modified from [16]).

6. Conclusions

(1) Controlled-source audio-frequency magnetotellurics was employed to infer the topography of the study area and convert it into coordinate data. The coordinates were adjusted using stratigraphic information obtained from drilling data. Geological modeling was conducted to reconstruct the paleokarst landform characteristics of the bauxite deposits in the Xiaoyuan area.

(2) The distribution of bauxite was influenced by ancient landforms. Horizontally, the bauxite grade was higher at the core of the karst depressions and lower in the surrounding area. The TiO_2 and SiO_2 contents had strong positive and negative correlations with the Al_2O_3 content, respectively. The Fe_2O_3 content was higher near the source area and lower farther away. Vertically, the bauxite in high-elevation regions showed a high iron content and low aluminum content, with a mineral assemblage comprising diaspore, siderite, anatase, and chlorite. Bauxite in low-elevation areas exhibited a lower iron content and a higher aluminum content, accompanied by a mineral assemblage consisting of diaspore, pyrite, illite, and anatase.

(3) Karst bauxite mineralization models for high-iron, low-aluminum contents and low-iron, high-aluminum contents were established. The former occurred in continental environments where the bauxite material rapidly accumulated in karst depressions at higher elevations. The latter was formed through modifications caused by seawater after the initial bauxite materials underwent sedimentation; this process typically occurred at lower elevations.

Supplementary Materials: The following supporting information can be downloaded at: https://www.mdpi.com/article/10.3390/min13081013/s1, Table S1: Resistivity values of representative stratigraphic and lithological samples in the research area and stratum thickness; Table S2: Major elements (%) of the Jiujialu Formation Al-bearing rock series in samples from the Xiaoyuan bauxite deposit. Table S3: Major (%), trace, and rare earth elements (ppm) of the Jiujialu Formation Al-bearing rock series, and underlying Cambrian Qingxudong Formation dolomite in samples from the Xiaoyuan bauxite deposit.

Author Contributions: Conceptualization, H.M. and R.Y.; methodology, H.M. and R.Y.; software, X.L. and C.L.; validation, Y.J.; investigation, H.M. and C.L.; resources, R.Y. and Z.Z.; data curation, H.M. and X.H.; writing—original draft preparation, H.M. and G.Y.; writing—review and editing, H.M. and X.Z.; visualization, C.G. and H.M.; supervision, R.Y.; project administration, R.Y.; funding acquisition, R.Y. and X.H. All authors have read and agreed to the published version of the manuscript.

Funding: This work was financially supported by the Project of Research, Development and Application of Key Technologies for Big Data Prediction of Bauxite Resources in Guizhou Province (No. [2022]ZD003-3), the National Natural Science Foundation of China (No. U1812402), and the Project of Scientific and Technological Innovation Team of Sedimentary Deposits in Guizhou Province (No. 2018-5613).

Data Availability Statement: Not applicable.

Conflicts of Interest: The authors declare no conflict of interest.

References

1. Gao, D.D.; Sheng, Z.Q.; Shi, S.H.; Chen, L.A. *Studies on the Bauxite Deposit in Central Guizhou*; Guizhou Science and Technology Publishing House: Guizhou, China, 1992; pp. 1–152. (In Chinese)
2. Ling, K.Y.; Zhu, X.Q.; Tang, H.S.; Wang, Z.G.; Yan, H.W.; Han, T.; Chen, W.Y. Mineralogical characteristics of the karstic bauxite deposits in the Xiuwen ore belt, Central Guizhou Province, Southwest China. *Ore Geol. Rev.* **2015**, *65*, 84–96. [CrossRef]
3. Long, Y.Z.; Chi, G.X.; Liu, J.P.; Jin, Z.G.; Dai, T.G. Trace and rare earth elements constraints in the sources of the Y unfeng paleo-karstic bauxite deposit in the Xiuwen-Qingzhen area, Guizhou, China. *Ore Geol. Rev.* **2017**, *91*, 404–418. [CrossRef]
4. Luo, C.K.; Yang, R.D.; Gao, J.B.; Muhammad, U.M.A.I.R.; Wang, L.B.; Gao, L. Viséan fossil plants from the Jiujialu Formation in central Guizhou Province: Implications for age of bauxite and palaeoenvironment. *Acta Geol. Sin.-Engl. Ed.* **2020**, *94*, 2165–2177. [CrossRef]

5. Luo, C.K.; Liang, P.; Yang, R.D.; Gao, J.B.; Chen, Q.; Mo, H.C. Mineralogical and Geochemical Constraints on the Occurrence Forms of REEs in Carboniferous Karst Bauxite, Central Guizhou Province, Southwest China: A Case Study of Lindai Bauxite. *Minerals* **2023**, *13*, 320. [CrossRef]
6. Wang, Q.F.; Deng, J.; Liu, X.F.; Zhang, Q.Z.; Li, Z.M.; Kang, W.; Cai, S.H.; Li, N. Review on research of bauxite geology and genesis in China. *Geol. Explor.* **2012**, *48*, 430–448.
7. Bárdossy, G. *Karst Bauxites: Bauxite Deposits on Carbonate Rocks*; Elsevier: Amsterdam, The Netherlands, 1982.
8. Yu, W.; Algeo, T.J.; Y an, J.; Y ang, J.; Du, Y.; Huang, X.; Weng, S. Climatic and hydrologic controls on upper Paleozoic bauxite deposits in South China. *Earth-Sci. Rev.* **2018**, *in press*. [CrossRef]
9. Li, P.G.; Yu, W.C.; Du, Y.S.; Lai, X.L.; Weng, S.F.; Pang, D.W.; Xiong, G.L.; Lei, Z.Y.; Zhao, S.; Yang, S.Q. Influence of geomorphology and leaching on the formation of Permian bauxite in northern Guizhou Province, South China. *J. Geochem. Explor.* **2020**, *210*, 106446. [CrossRef]
10. Wang, Q.F.; Liu, X.F.; Yang, S.J.; Zhang, Q.Z.; Deng, J. How is karst type bauxite formed? *Earth Sci.* **2022**, *47*, 3880–3881. (In Chinese)
11. D'Argenio, B.; Mindszenty, A. Bauxites and related paleokarst: Tectonic and climatic event markers at regional unconformities. *Eclogae Geol. Helv.* **1995**, *88*, 453–499.
12. Cheng, P.L.; Li, S.N.; Chen, Q.; Wu, X.H. The genesis of the bauxite deposit in central Guizhou is discussed based on the output characteristics of high iron bauxite in Maochang mining area of Qingzhen. *Guizhou Geol.* **2004**, *4*, 215–222. (In Chinese)
13. Valeton, I. *Saprolite-Bauxite Facies of Ferralitic Duricrusts on Palaeosurfaces of Former Pangaea, Palaeoweathering, Palaeosurfaces and Related Continental Deposits*; Blackwell Publishing Ltd.: Hoboken, NJ, USA, 2009; pp. 153–188.
14. Liu, P.; Han, Z.H.; Nie, K. Characteristics of ore-bearing rock series, control conditions and generative development model of karst bauxite deposit in central Guizhou—southern Chongqing. *Geol. Rev.* **2022**, *68*, 11. [CrossRef]
15. Wang, R.X.; Wang, Q.F.; Huang, Y.X.; Yang, S.J.; Liu, X.F.; Zhou, Q. Combined tectonic and paleogeographic controls on the genesis of bauxite in the early Carboniferous to Permian Central Yangtze Island. *Ore Geol. Rev.* **2018**, *101*, 468–480. [CrossRef]
16. Luo, C.K.; Yang, R.D.; Chen, J.; Gao, L.; Xu, H.; Ni, X.R. Genesis of the Carboniferous karstic bauxites in Qingzhen region, central Guizhou, southwest China. *J. Geochem. Explor.* **2022**, *235*, 106955. [CrossRef]
17. Deng, X.; Yang, K.G.; Liu, Y.L.; She, Z.B. Characteristics and tectonic evolution of Qianzhong Uplift. In *Earth Science Frontiers*; China University of Geosciences (Beijing); Peking University: Beijing, China, 2010; Volume 13, pp. 79–89. (In Chinese)
18. Liu, W.; Xu, X.S.; Yu, Q. Discussion on forming mechanism and evolution of the central Guizhou Palaeouplift. *Acta Sedimentol. Sin.* **2011**, *29*, 658–664. (In Chinese with English Abstract)
19. Tang, L.J.; Guo, T.L.; Tian, H.Q.; Jin, W.Z.; Li, R.F.; Wan, G.M.; Dong, L.; Wang, P.W. Poly-cycle tectonic evolution, differential deformation and hydrocarbon reservation of Central Guizhou and adjacent region. *Acta Geol. Sin.* **2008**, *82*, 298–307, (In Chinese with English Abstract).
20. GBGM (Guizhou Bureau of Geology and Minerals). *Geological Marks of Guizhou Province*; Geological Publishing House: Beijing, China, 1987; pp. 1–360. (In Chinese)
21. Gan, T.; Luo, T.Y.; Pang, K.; Zhou, C.M.; Zhou, G.H.; Wan, B.; Li, G.; Yi, Q.R.; Czaja, A.D.; Xiao, S.H. Cryptic terrestrial fungus-like fossils of the early Ediacaran Period. *Nat. Commun.* **2021**, *12*, 641. [CrossRef]
22. Liao, Q.T. Characteristics and application range of V8 multifunctional electrical measurement system. *Resour. Environ. Eng.* **2008**, *22*, 150–153. (In Chinese) [CrossRef]
23. Yan, W.H.; Liu, Y.F.; You, L.Q. The application of comprehensive geophysical prospecting method to exploring a certain zinc and lead deposit in northwest Guizhou Province. *Geophys. Geochem. Explor.* **2016**, *40*, 688–694. [CrossRef]
24. Jin, R.G.; Zhang, J.H.; Wang, Q.S. Research on the method and technology of magneticprospecting method using V8 systems. *China Min. Mag.* **2016**, *25*, 146–149.
25. Wang, L. *AMT Forwarding Modeling and Inversion Algorithms and Software Development*; Central South University: Changsha, China, 2013.
26. Zhao, G.Z.; Liu, G.D. An inversion method on two-dimensional magnetotelluric model. *Seismol. Geol.* **1985**, *7*, 56–58.
27. Deng, X.S.; Du, Y.S.; Yu, W.C.; Wu, K.B.; Lu, S.F.; Zhang, H.B. Qianzhong Uplift'and evolution of the Late Paleozoic palaeogeography and its control on formation of bauxite in Guizhou Province. *J. Palaeogeogr. (Chin. Ed.)* **2020**, *22*, 5.
28. Saad, R.; Nawawi, M.N.M.; Mohamad, E.T. Groundwater detection in alluvium using 2-D electrical resistivity tomography (ERT). *Electron. J. Geotech. Eng.* **2012**, *17*, 369–376.
29. Wang, X.B. *Application Study of High-Density Resistivity Imaging Method in the Quaternary Lithology of Juye River Basin*; Shandong Agricultural University: Tai'an, China, 2020. [CrossRef]
30. Zhang, Z.W.; Zhou, L.J.; Li, Y.J.; Wu, C.Q.; Zheng, C.F. The "coal-bauxite-iron" structure in the ore-bearing rock series as a prospecting indicator for southeastern Guizhou bauxite mines. *Ore Geol. Rev.* **2013**, *53*, 145–158. [CrossRef]
31. Yang, R.D.; Gao, J.B.; Zhao, K.; Yu, J.L.; Zhu, C.L.; Gao, L.; Chen, J.Y.; Zhou, R.X. Roof and Floor Characteristics of Bauxite in Qingzhen, Guizhou and Its Implication for Bauxite Mineralization. *Acta Geol. Sinca* **2018**, *92*, 2155–2165. (In Chinese with English Abstract)
32. Ahmadnejad, F.; Zamanian, H.; Taghipour, B.; Zarasvandi, A.; Buccione, R.; Ellahi, S.S. Mineralogical and geochemical evolution of the Bidgol bauxite deposit, Zagros Mountain Belt, Iran: Implications for ore genesis, rare earth elements fractionation and parental affinity. *Ore Geol. Rev.* **2017**, *86*, 755–783. [CrossRef]

33. Liu, X.F.; Wang, Q.F.; Feng, Y.W.; Li, Z.M.; Cai, S.H. Genesis of the Guangou karstic bauxite deposit in western Henan, China. *Ore Geol. Rev.* **2013**, *55*, 162–175. [CrossRef]
34. Liu, X.F.; Wang, Q.F.; Zhao, L.H.; Peng, Y.B.; Ma, Y.; Zhou, Z.H. Metallogeny of the large-scale Carboniferous karstic bauxite in the Sanmenxia area, southern part of the North China Craton, China. *Chem. Geol.* **2020**, *556*, 119851. [CrossRef]
35. Zhang, L.; Park, C.; Wang, G.H.; Wu, C.J.; Santosh, M.; Chung, D.; Song, Y. Phase transformation processes in karst-type bauxite deposit from Yunnan area, China. *Ore Geol. Rev.* **2017**, *89*, 407–420. [CrossRef]
36. Yang, S.J.; Huang, Y.X.; Wang, Q.F.; Deng, J.; Liu, X.F.; Wang, J.Q. Mineralogical and geochemical features of karst bauxites from Poci (western Henan, China), implications for parental affinity and bauxitization. *Ore Geol. Rev.* **2019**, *105*, 295–309. [CrossRef]
37. Zhang, J.Y.; Wang, Q.F.; Liu, X.F.; Zhou, G.F.; Xu, H.P.; Zhu, Y.G. Provenance and ore-forming process of Permian lithium-rich bauxite in central Yunnan, SW China. *Ore Geol. Rev.* **2022**, *145*, 104862. [CrossRef]
38. Liu, X.F.; Wang, Q.F.; Zhang, Q.Z.; Yang, S.J.; Liang, Y.Y.; Zhang, Y.; Li, Y.; Guan, T. Genesis of the Permian karstic Pingguo bauxite deposit, western Guangxi, China. *Miner. Depos.* **2017**, *52*, 1031–1048. [CrossRef]
39. Wang, R.X.; Wang, Q.F.; Uysal, I.T.; Ramanaidou, E.; Deng, J.; Todd, A. Mesozoic hydrothermal overprint on carboniferous bauxite in China. *Econ. Geol.* **2021**, *116*, 787–800. [CrossRef]
40. Wang, R.X. *Mineral Compositions and Metallogenic Mechanism of Important Bauxite Concentration Areas in China*; China University of Geosciences Beijing: Beijing, China, 2019.
41. Xing, B.B.; Graham, N.; Yu, W.Z. Transformation of siderite to goethite by humic acid in the natural environment. *Commun. Chem.* **2020**, *3*, 38. [CrossRef] [PubMed]
42. Zamanian, H.; Ahmadnejad, F.; Zaravandi, A. Mineralogical and geochemical investigations of the Mombi bauxite deposit, Zagros Mountains, Iran. *Chem. Der Erde* **2016**, *73*, 13–37. [CrossRef]
43. Ling, K.Y.; Zhu, X.Q.; Tang, H.S.; Li, S.X. Importance of hydrogeological conditions during formation of the karstic bauxite deposits, Central Guizhou Province, Southwest China: A case study at Lindai deposit. *Ore Geol. Rev.* **2017**, *82*, 198–216. [CrossRef]
44. Sun, J.H.; Chen, Q.Y. Mineral composition of bauxite in central Guizhou province. *Sci. Geol. Sin.* **1992**, 226–237.
45. Bárdossy, G.; Aleva, G.J.J. *Lateritic Bauxites*; Elsevier Scientific Publication: Amsterdam, The Netherlands, 1990; pp. 1–624.
46. Wang, E.F. The origin of red high iron bauxite in some mining areas in Paleozoic. *Light Met.* **1982**, *9*, 1–6. (In Chinese)
47. Liu, P.; Liao, Y.C. The zonation and genetic mechanism of Zunyi high-and low-ferrous bauxites. *Geol. China* **2013**, *40*, 949–966.
48. Ling, K.Y.; Wen, H.J.; Fan, H.F.; Zhu, X.K.; Li, Z.H.; Zhang, Z.W.; Stephen, E.G. Iron loss during continental weathering in the early Carboniferous period recorded by karst bauxites. *J. Geophys. Res. Earth Surf.* **2023**, *128*, e2022JF006906. [CrossRef]
49. Vincent, G.; Vincent, O.; Olivier, B.; Cécile, M.; Esmaeil, S.; Jules, F.; Lucilla, B.; Valéry, G. Weathering-limited hillslope evolution in carbonate landscapes. *Earth Planet. Sci. Lett.* **2016**, *446*, 10–20, ISSN 0012-821X. [CrossRef]
50. Laskou, M.; Economou-Eliopoulos, M. The role of microorganisms on the mineralogical and geochemical characteristics of the Parnassos-Ghiona bauxite deposits, Greece. *J. Geochem. Explor.* **2007**, *93*, 67–77. [CrossRef]
51. Liu, X.F.; Wang, Q.F.; Deng, J.; Zhang, Q.Z.; Sun, S.L.; Meng, J.Y. Mineralogical and geochemical investigations of the Dajia Salento-type bauxite deposits, western Guangxi, China. *J. Geochem. Explor.* **2010**, *105*, 137–152. [CrossRef]
52. Jin, Z.G.; Liu, C.S.; Zhou, L.; Zheng, M.H.; Zhang, L.; Han, Y. Geochemical evidence of sedimentary environment of permian bauxite in the Wuchuan-Zheng'an-Daozhen area, Guizhou province. *Acta Geol. Sin.* **2018**, *92*, 817–827.
53. Abedini, A.; Khosravi, M. Geochemical constraints on the Triassic–Jurassic Amir-Abad karst-type bauxite deposit, NW Iran. *J. Geochem. Explor.* **2020**, *211*, 106489. [CrossRef]
54. Abedini, A.; Mongelli, G.; Khosravi, M.; Sinisi, R. Geochemistry and secular trends in the middle–late Permian karst bauxite deposits, northwestern Iran. *Ore Geol. Rev.* **2020**, *124*, 103660. [CrossRef]
55. Abedini, A.; Mongelli, G.; Khosravi, M. Geochemical constraints on the middle Triassic Kani Zarrineh karst bauxite deposit, Irano–Himalayan belt, NW Iran: Implications for elemental fractionation and parental affinity. *Ore Geol. Rev.* **2021**, *133*, 104099. [CrossRef]
56. Liu, Y.J.; Cao, L.M.; Li, Z.L.; Wang, H.N.; Chu, T.Q.; Zhang, Y.R. *Geochemistry of the Elements*; Science Press: Beijing, China, 1986; pp. 1–386. (In Chinese)
57. Nesbitt, H.W. Mobility and fractionation of rare earth elements during weathering of a granodiorite. *Nature* **1979**, *279*, 206–210. [CrossRef]
58. Duddy, L.R. Redistribution and fractionation of rare-earth and other elements in a weathering profile. *Chem. Geol.* **1980**, *30*, 363–381. [CrossRef]
59. Ji, H.B.; Wang, S.J.; Ouyang, Z.Y.; Zhang, S.; Sun, C.X.; Liu, X.M.; Zhou, D.Q. Geochemistry of red residua underlying dolomites in karst terrains of Yunnan-Guizhou Plateau II. The mobility of rare earth elements during weathering. *Chem. Geol.* **2004**, *203*, 29–50. [CrossRef]
60. Mongelli, G. Ce-anomalies in the textural components of Upper Cretaceous karst bauxites from the Apulian carbonate platform (southern Italy). *Chem. Geol.* **1997**, *140*, 69–79. [CrossRef]
61. Khosravi, M.; Abedini, A.; Alipour, S.; Mongelli, G. The Darzi-Vali bauxite deposit, West-Azarbaidjan Province, Iran: Critical metals distribution and parental affinities. *J. Afr. Earth Sci.* **2017**, *129*, 960–972. [CrossRef]
62. Abedini, A.; Mongelli, G.; Khosravi, M. Geochemistry of the early Jurassic Soleiman Kandi karst bauxite deposit, Irano–Himalayan belt, NW Iran: Constraints on bauxite genesis and the distribution of critical raw materials. *J. Geochem. Explor.* **2022**, *241*, 107056. [CrossRef]

63. Meshram, R.R.; Randive, K.R. Geochemical study of laterites of the Jamnagar district, Gujarat, India: Implications on parent rock, mineralogy and tectonics. *J. Asian Earth Sci.* **2011**, *42*, 1271–1287. [CrossRef]
64. Braun, J.J.; Pagel, M.; Herbilln, A.; Rosin, C. Mobilization and redistribution of REEs and thorium in a syenitic lateritic profile: A mass balance study. *Geochim. Et Cosmochim. Acta* **1993**, *57*, 4419–4434. [CrossRef]
65. Mameli, P.; Mongelli, G.; Oggiano, G.; Dinelli, E. Geological, geochemical and mineralogical features of some bauxite deposits from Nurra (Western Sardinia, Italy): Insights on conditions of formation and parental affinity. *Int. J. Earth Sci.* **2007**, *96*, 887–902. [CrossRef]
66. Wang, T.S.; Fu, Y.; Chen, P.W.; Hou, K.J.; Tang, B.; Luo, P.Q.; Yao, L.; Liu, B.; Long, Z.; Liu, Y.; et al. Detrital composition and sedimentary provenance of Early Carboniferous Al-bearing rock series in central Guizhou. *Ore Geol. Rev.* **2023**, *156*, 105404. [CrossRef]
67. Franceschelli, M.; Puxeddu, M.; Memmi, I. Li, B-rich Rhaetian metabauxite, Tuscany, Italy: Reworking of older bauxites and igneous rocks. *Chem. Geol.* **1998**, *144*, 221–242. [CrossRef]
68. Wang, Q.F.; Liu, X.F.; Yan, C.H.; Cai, S.H.; Li, Z.M.; Wang, Y.R.; Zhao, J.M.; Li, G.J. Mineralogical and geochemical studies of boron-rich bauxite ore deposits in the Songqi region, SW Henan, China. *Ore Geol. Rev.* **2012**, *48*, 258–270. [CrossRef]
69. De Bussetti, S.G.; Ferreiro, E.A.; Helmy, A.K. Sorption of Boron by Hydrous Al-Oxide. *Clays Clay Min.* **1995**, *43*, 58–62. [CrossRef]
70. Xiao, R.G.; Takao, O.; Cai, K.Q.; Yoshikazu, K. Application of boron and boron isotopic geochemistry in the study of geological process. In *Earth Science Frontiers*; China University of Geosciences: Beijing, China, 1999; Volume 2, pp. 168–175.
71. Wang, X.J.; Wang, Z.T.; Wang, G.H.; Zhou, J.; Cui, Y.L.; Zhang, D.H. Geochemical characteristics and ore-forming environment of the Songgui bauxite deposit in Heqing county, Northwest Yunnan province. *Northwestern Geol.* **2017**, *50*, 205–221.
72. Yu, W.C.; Du, Y.S.; Gu, S.Z.; Cui, T.; Huang, X.; Yu, J.X.; Qin, Y.J.; Lei, Z.Y.; Weng, S.F.; Cao, J.Z. Multiperiod leaching process of early Permian bauxitein Wuchuan-Zheng'an-Daozhen area, northern Guizhou province and its significance of ore control. *Geol. Sci. Technol. Inf.* **2013**, *32*, 34–39.
73. Barrat, J.A.; Taylor, R.N.; André, J.P.; Nesbitt, R.W.; Lecuyer, C. Strontium isotopes in biogenic phosphates from a neogene marine formation: Implications for palaeoseawater studies. *Chem. Geol.* **2000**, *168*, 325–332, ISSN 0009-2541. [CrossRef]
74. Feng, X.L.; Long, J.Z. A genetic model for the Maochang bauxite depositin in central Guizhou. *Guizhou Geol.* **1997**, *14*, 285–298.
75. Sun, S.S.; McDonough, W.F. Chemical and isotopic systematics of oceanic basalts: Implications for mantle composition and processes. *Geol. Soc. Lond. Spec. Publ.* **1989**, *42*, 313–345. [CrossRef]
76. Yin, Z.M. The Texture and Structure features of Carboniferous Bauxite in China and Its Emplacement Mechanism. *J. Cent. South Univ. Min. Metall.* **1988**, *19*, 357–363.
77. Yu, W.C.; Wang, R.H.; Zhang, Q.L.; Du, Y.S.; Chen, Y.; Liang, Y.P. Mineralogical and geochemical evolution of the fusui bauxite deposit in Guangxi, south China: From the original Permian orebody to a Quarternary salento-type deposit. *J. Geochem. Explor.* **2014**, *146*, 75–88. [CrossRef]